J. Fluid Mech. (2011), *vol.* 685, *pp.* 495–531.
doi:10.1017/jfm.2011.337

Experimental study of three-scalar mixing in a turbulent coaxial jet

J. Cai[1], M. J. Dinger[1], W. Li[1], C. D. Carter[2], M. D. Ryan[2] and C. Tong[1]†

[1] Department of Mechanical Engineering, Clemson University, Clemson, SC 29634, USA

[2] Air Force Research Laboratory, Wright-Patterson Air Force Base, Dayton, OH 45433, USA

(Received 9 October 2010; revised 17 May 2011; accepted 3 August 2011;
first published online 19 September 2011)

In the present study we investigate three-scalar mixing in a turbulent coaxial jet. In this flow a centre jet and an annular flow, consisting of acetone-doped air and ethylene respectively, are mixed with the co-flow air. A unique aspect of this study compared to previous studies of three-scalar mixing is that two of the scalars (the centre jet and air) are separated by the third (annular flow); therefore, this flow better approximates the mixing process in a non-premixed turbulent reactive flow. Planar laser-induced fluorescence and Rayleigh scattering are employed to measure the mass fractions of the acetone-doped air and ethylene. The results show that the most unique aspects of the three-scalar mixing occur in the near field of the flow. The mixing process in this part of the flow are analysed in detail using the scalar means, variances, correlation coefficient, joint probability density function (JPDF), conditional diffusion, conditional dissipation rates and conditional cross-dissipation rate. The diffusion velocity streamlines in scalar space representing the conditional diffusion generally converge quickly to a manifold along which they continue at a lower rate. A widely used mixing model, interaction through exchange with mean, does not exhibit such a trend. The approach to the manifold is generally in the direction of the ethylene mass fraction. The difference in the magnitudes of the diffusion velocity components for the two scalars cannot be accounted for by the difference in their dissipation time scales. The mixing processes during the approach to the manifold, therefore, cannot be modelled by using different dissipation time scales alone. While the three scalars in this flow have similar distances in scalar space, mixing between two of the scalars can occur only through the third, forcing a detour of the manifold (mixing path) in scalar space. This mixing path presents a challenging test for mixing models since most mixing models use only scalar-space variables and do not take into account the spatial (physical-space) scalar structure. The scalar JPDF and the conditional dissipation rates obtained in the present study have similarities to those of mixture fraction and temperature in turbulent flames. The results in the present study provide a basis for understanding and modelling multiscalar mixing in reactive flows.

Key words: jets, turbulent mixing

† Email address for correspondence: ctong@ces.clemson.edu

1. Introduction

Turbulent mixing of scalar quantities is of great importance for a range of engineering and environmental applications such as combustion, industrial chemical production, and pollutant dispersion in the atmosphere. These applications depend on turbulence to mix scalar quantities rapidly, often at rates orders of magnitude higher than in laminar flows. It is, therefore, of interest to understand the physics of turbulent mixing, and to predict the mixing processes. In some applications, such as pollutant dispersion, a single scalar is mixed with a background flow. The mixing process is binary in nature and has been studied extensively. In many other applications, such as reactive flows, at least three scalars are involved. Thus the mixing process is inherently multiscalar, and is more complex. In spite of its importance, multiscalar mixing has received much less attention. In the present study, we investigate several important aspects of three-scalar mixing.

Much of our understanding of turbulent mixing is based on binary (two-scalar) mixing. Many experimental and numerical studies focused on the basic statistics characterizing the evolution of scalar fields, such as the mean scalar, the scalar variance, and the scalar dissipation time scale in various flows (e.g. Warhaft & Lumley 1978; Sreenivasan *et al.* 1980; Antonopoulos-Domis 1981; Ma & Warhaft 1986; Eswaran & Pope 1988; Jayesh & Warhaft 1992; Overholt & Pope 1996). A number of other works studied the scalar probability density function (PDF) and the PDF transport equation (e.g. Eswaran & Pope 1988; Tong & Warhaft 1995). The scalar PDF is important for characterizing scalar mixing in many applications, such as pollutant dispersion, where in addition to the scalar mean and variance, the probability for the pollutant concentration to exceed a given level (e.g. a threshold) must be known for environmental and health concerns. The scalar PDF is also important for studying and modelling turbulent reactive flows because reaction rates generally have highly nonlinear dependences on species concentrations.

The mixing process that evolves the PDF, f_ϕ, of a scalar variable, ϕ, can be studied using the PDF transport equation (Pope 1985),

$$\frac{\partial f_\phi}{\partial t} + \frac{\partial}{\partial x_i}[f_\phi(U_i + \langle u_i \mid \hat{\phi}\rangle)] = -\frac{\partial}{\partial \hat{\phi}}\{f_\phi[\langle D\nabla^2\phi \mid \hat{\phi}\rangle + S(\hat{\phi})]\}$$
$$= D\nabla^2 f_\phi - \frac{1}{2}\frac{\partial^2}{\partial \hat{\phi}^2}(f_\phi\langle \chi \mid \hat{\phi}\rangle) - \frac{\partial}{\partial \hat{\phi}}[f_\phi S(\hat{\phi})], \quad (1.1)$$

where U_i, u_i and S are the mean and fluctuating velocities and the reaction rate, respectively. The left-hand side is the time rate of change of the PDF and transport of the PDF in physical space by turbulent velocity. The right-hand side gives two forms of the mixing term. They involve the conditional scalar diffusion, $\langle D\nabla^2\phi \mid \phi = \hat{\phi}\rangle$, and the conditional scalar dissipation, $\langle \chi \mid \phi = \hat{\phi}\rangle = \langle 2D(\partial\phi/\partial x_i)(\partial\phi/\partial x_i) \mid \phi = \hat{\phi}\rangle$, respectively, where the angle brackets denote an ensemble average. For convenience we omit the sample space variable $\hat{\phi}$ hereafter. The mixing term represents the effects of turbulent mixing on the evolution of the scalar PDF and is unclosed. The last term is the reaction source term and is closed. The success of PDF methods (Pope 1985), which solve the scalar PDF transport equation, in predicting reactive flows comes from exact treatment of the reaction rate term. In homogeneous scalar fields, the terms containing spatial derivatives of statistics vanish, but the conditional diffusion or scalar dissipation does not. It is, therefore, of importance to study the physics of turbulent mixing in terms of the PDF equation.

Passive scalar PDFs have been studied in various types of flows. A range of PDF forms have been observed, including bimodal (e.g. Eswaran & Pope 1988; Dahm & Dimotakis 1990), near Gaussian and quasi- (or skewed) Gaussian (e.g. Venkataramani, Tutu & Chevray 1975; Sreenivasan & Antonia 1978; Venkataramani & Chevray 1978; Lockwood & Moneib 1980; Tavoularis & Corrsin 1981; Drake, Pitz & Shyy 1986; Tong & Warhaft 1995), and exponential tails (e.g. Jayesh & Warhaft 1991, 1992; Pumir, Shraiman & Siggia 1991; Holzer & Pumir 1993; Shraiman & Siggia 1994; Kerstein & McMurtry 1994; Jaberi *et al.* 1996*a*). Various models such as the 'clipped Gaussian' (Lockwood & Naguib 1975), the beta model (e.g. Rhodes 1975; Janicka & Kollmann 1979), and the composite model of Effelsberg & Peters (1983) have been used to approximate the scalar PDF.

The conditional scalar dissipation, $\langle \chi \mid \phi \rangle$, has been shown in general to be dependent on the value of ϕ. In direct numerical simulation (DNS) of homogeneous binary scalar mixing, the conditional dissipation was found to be generally bell-shaped (Eswaran & Pope 1988; Gao 1991; O'Brien & Jiang 1991; Miller *et al.* 1993). Measurements of Jayesh & Warhaft (1991, 1992) in isotropic grid turbulence with a constant mean scalar gradient, on the other hand, found concave upward conditional dissipation. Analytical works (e.g. Sinai & Yahkot 1989; O'Brien & Jiang 1991; Miller *et al.* 1993; Pope & Ching 1993; Sahay & O'Brien 1993; Sabel'nikov 1998) have linked the conditional dissipation in homogeneous scalar fields to the scalar PDF. In inhomogeneous flows the dependence is more complex. Measurements in turbulent jets (e.g. Kailasnath, Sreenivasan & Saylor 1993; Mi, Antonia & Anselmet 1995; Tong & Warhaft 1995) and in turbulent wakes and boundary layers (e.g. Kailasnath *et al.* 1993) showed that the conditional dissipation is strongly dependent on the flow type as well as the position of the measurement location in the flow.

The conditional scalar diffusion $\langle D\nabla^2\phi \mid \phi \rangle$ in DNS with homogeneous scalar fluctuations was found to be linear in ϕ at large times (Leonard & Hill 1991; Miller *et al.* 1993; Overholt & Pope 1996; Yeung 1998) but S-shaped at small times (Miller *et al.* 1993). Jaberi, Miller & Givi (1996*b*) showed that for scalar fields with zero mean gradient, this linear dependence can be derived from self-similar scalar PDFs. For a constant scalar gradient, Sabel'nikov (1998) showed that for self-similar PDFs the conditional diffusion has a linear dependence on both the scalar and the conditional velocity, $\langle u_j|\phi \rangle$. Measurements in inhomogeneous shear flows showed that the conditional diffusion is approximately linear near the centreline of a wake (Kailasnath *et al.* 1993) and a jet (Tong & Warhaft 1995), and is approximately piecewise linear off the jet centreline (Tong & Warhaft 1995). Thus, the large-scale structures in shear flows have a strong influence on the conditional diffusion.

In reactive flows there are often at least three scalars involved, e.g. two reactants and one product. It is, therefore, of importance to study multiscalar mixing, the simplest case being three-scalar mixing. In contrast to the large number of studies on two-scalar mixing, there are few previous studies on three-scalar mixing. Warhaft (1981) extended the study of Warhaft & Lumley (1978) to three scalars using two mandolines to study the evolution of the correlation coefficient between the two scalars, and found that it is initially high (positive) and decays downstream. Sirivat & Warhaft (1982) conducted a three-scalar experiment in decaying grid turbulence where two scalars were injected into the background air flow (the third scalar). The scalar r.m.s. decays faster with decreasing initial scalar length scales. They also measured the correlation coefficient between the two scalars. The evolution of the correlation depends on the way the scalars were introduced. The asymptotic values range from close to negative one to positive one. Warhaft (1984) used two line sources to introduce two scalars

into decaying grid turbulence. He measured the correlation coefficient between the two scalars and found that it starts from close to zero and becomes negative further downstream before approaching unity eventually. Tong & Warhaft (1995) extended this experiment to a turbulent jet, finding a similar evolution of the correlation coefficient. Extending the study by Eswaran & Pope (1988) to three scalars arranged symmetrically in scalar space and physical space, Juneja & Pope (1996) studied the mixing in statistically stationary, homogeneous, and isotropic turbulence. They found that the early mixing is between pairs of blobs. The scalar joint PDF (JPDF) later becomes uniform before finally taking a shape close to Gaussian at large times.

In three-scalar mixing problems, the arrangement of the initial scalar configuration is important. In Sirivat & Warhaft (1982), Warhaft (1984) and Tong & Warhaft (1995), two of the scalars were introduced into a background scalar (air), whereas in Juneja & Pope (1996) the three scalars were arranged symmetrically. To understand better the mixing scenario in turbulent non-premixed reactive flows, we study three-scalar mixing in a coaxial jet emanating into co-flow air. In this flow the scalar from the centre jet (ϕ_1) and the co-flow air at the jet exit plane are separated by the scalar from the annulus (ϕ_2). As a result, initially there is direct mixing between ϕ_1 and ϕ_2 and between ϕ_2 and air but not between ϕ_1 and air. Mixing between ϕ_1 and air must involve ϕ_2. This mixing configuration represents better the mixing process in turbulent non-premixed reactive flows where mixing between reactants generally must involve the product.

The present work aims to gain an understanding of the physics of three-scalar mixing. Measurements in a turbulent coaxial jet are made using planar laser induced fluorescence (PLIF) and planar laser Rayleigh scattering. We present the basic statistics characterizing the mixing process, such as the scalar means, r.m.s. fluctuations, cross-correlation coefficient, segregation parameter and scalar dissipation rates. We also analyse the scalar JPDF and the mixing terms evolving the JPDF. To aid model development, the results are contrasted with the IEM (interaction through exchange with the mean) mixing model to highlight the important aspects of the mixing process and the deficiencies of the model. Previous works on a coaxial jet (e.g. Buresti, Petagna & Talamelli 1998; Villermaux & Rehab 2000; Balarac *et al.* 2007) only studied mixing of a single scalar introduced into either the centre jet or the annular flow; therefore, the mixing problem is still binary in nature. The rest of the paper is organized as follows. Section 2 describes the experimental setup and data analysis procedures. Section 3 presents the results followed by the conclusions and Appendix.

2. Experimental facilities and data analysis procedures

2.1. *Flow facilities and measurement system*

The coaxial jet in the present study consisted of a centre tube and an annulus (figure 1). The jet tubes have ends with 90° corners produced by a shape cut. Both tubes have sufficient lengths such that the flows at their exits were close to fully developed pipe and annular flows, respectively. Thus the downstream flow is not expected to be sensitive to the geometrical details of the tubes. Both streams issued into co-flow air with a velocity of $\approx$0.4 m s^{-1}. The co-flow has a diameter of 150 mm, sufficiently large that the ambient air does not interact with the jet for the downstream locations studied. The flow was exhausted by a collection hood at $\approx$100 annulus diameters downstream of the jet. The centre jet flow was air seeded with $\approx$7 % of acetone by volume and the annulus stream was ethylene. The densities

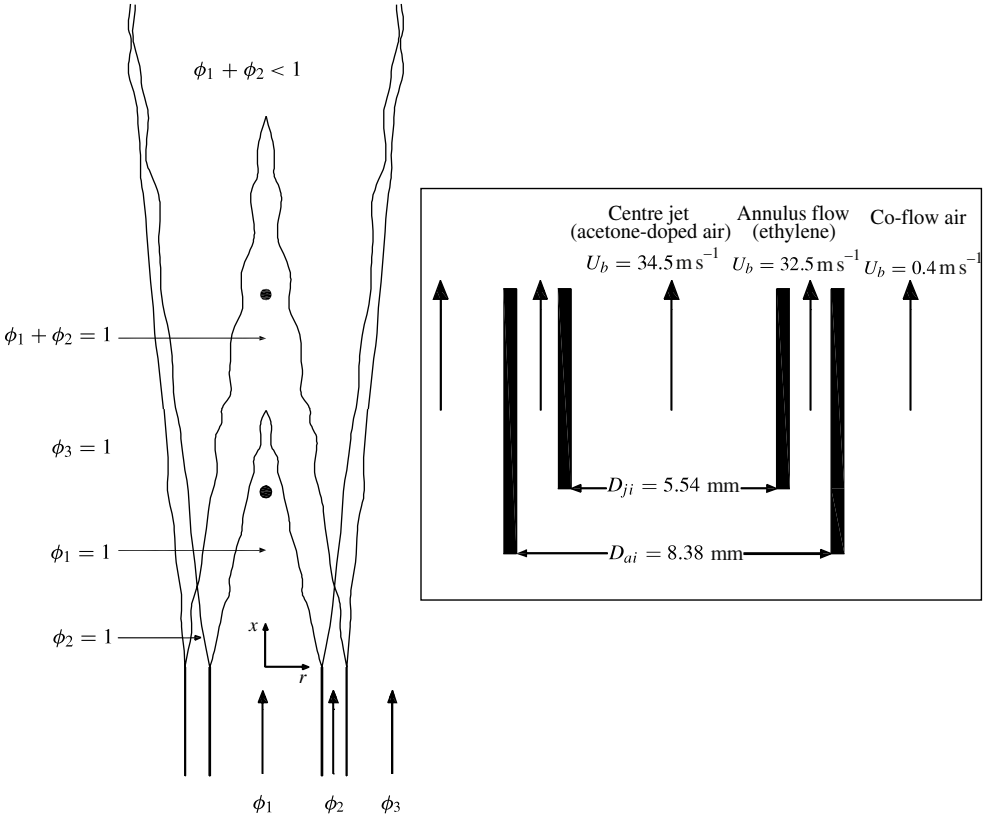

FIGURE 1. Schematic of the coaxial jet. The scalar values are normalized at the jet exit. The different stages of the evolution of the scalar fields are shown qualitatively. The approximate downstream locations, at which detailed results are given in § 3, are indicated by solid circles.

of the acetone-doped air and ethylene were ≈1.07 and 0.966 times the air density. These differences are sufficiently small for the scalars to be considered dynamically passive. The jet dimensions and velocities are listed in table 1. The Reynolds numbers are obtained as $Re_j = U_{jb}D_{ji}/\nu_{air}$ and $Re_a = U_{ab}(D_{ai} - (D_{ji} + 2\delta_j))/\nu_{eth}$, where $\nu_{air} = 1.56 \times 10^{-5}$ m^2 s^{-1} and $\nu_{eth} = 0.86 \times 10^{-5}$ m^2 s^{-1} (Prausnitz, Poling & O'Connell 2001) are the kinematic viscosities of air and ethylene respectively. The acetone mass concentration is normalized by its value at the jet exit, so ϕ_1, which represents the scalar from the centre jet, has a value of unity at the exit. The normalized concentration of ethylene (ϕ_2) at the annulus exit is also unity since this stream is pure ethylene.

The source of the air was a facility compressor, while the source of the ethylene was chemically pure ethylene in a gas cylinder. Air and ethylene flow rates were controlled with Tylan mass flow controllers. Good accuracy for the indicated flow rates was ensured by using a Bios DryCal piston-type calibrator. Both gas streams were filtered for particles before entering the flow controllers. Spectroscopic grade acetone was seeded into the air stream by bubbling the air through a sealed Teflon container with acetone liquid. This container was placed in a room temperature water bath to help maintain the acetone vapour pressure. Because the acetone concentration could not be controlled easily, a sample line was set up to feed a reference jet for monitoring

Inner tube				Annulus				Co-flow
D_{ji} (mm)	δ_j (mm)	U_{jb} (m s^{-1})	Re_j	D_{ai} (mm)	δ_a (mm)	U_{ab} (m s^{-1})	Re_a	U (m s^{-1})
5.54	0.406	34.5	12 190	8.38	0.559	32.5	7 636	0.4

TABLE 1. Characteristics of the coaxial jet. Here δ_j, δ_a, U_{jb} and U_{ab} are the wall thicknesses and the bulk velocities of the centre tube and the annulus, respectively. The Reynolds numbers are calculated using the tube diameter D_{ji} and the hydraulic diameter of the annulus $D_{ai} - (D_{ji} + 2\delta_j)$, respectively.

the upstream acetone concentration to normalize the concentration and laser beam profile. The uncertainties in determining the acetone source concentration are discussed in Appendix B.

The number densities of the acetone and ethylene were measured using PLIF and planar laser Rayleigh scattering techniques. Two Q-switched Nd:YAG lasers were employed: a Quanta-Ray GCR-4 delivering ≈600 mJ pulse^{-1} at 532 nm was used for ethylene Rayleigh scattering, while a Quanta-Ray GCR-150 delivering ≈75 mJ pulse^{-1} at 266 nm was used for acetone PLIF. The frequency-doubled output of the GCR-150 was itself frequency-doubled in a BBO crystal housed within a heater. The 532 and 266 nm beams were then separated within a Pellin–Broca prism (figure 2). In each case a collimated laser probe sheet was formed with a telescope consisting of a negative cylindrical lens (−100 and −150 mm focal lengths, respectively, for the 266 and 532 nm beams) followed by a 1 m focal length spherical lens. The two sheets were combined onto the same path using a dielectric mirror designed to reflect 266 nm radiation and pass 532 nm radiation. The focus for both laser sheets was approximately located at the jet centreline. Sheet widths were measured by translating a 25 μm slit across the laser sheet and measuring the transmitted portion of the beam with a photodiode. Sheet thicknesses were about 100 and 200 μm, respectively, for the 226 and 532 nm beams. The laser sheet heights were around 50 mm and were approximately constant, but only the central 25 mm was imaged where the beam had the highest intensity.

The PLIF and planar Rayleigh scattering images were collected by a Cooke Corp. PCO-1600 interline-transfer CCD camera. The laser pulses were separated by 250 ns (with the GCR-4 laser used for Rayleigh scattering firing first), and straddled the transfer time for the CCD camera. This time separation is sufficiently short for the flow speed (less than 35 m s^{-1}). This camera has an array of 1600 × 1200 pixels (each 7.4 μm^2); pixels were binned 2 × 2 before readout, and the array was further cropped such that the effective size was 800 pixels wide by 450 pixels high with a resulting field of view of 24.8 mm (high) × 44.1 mm (wide). This array size ensured that both frames could be read within 0.1 s, the period for the laser firing cycles. Timing was controlled by a LabSmith LC880 Programmable Logic Controller and monitored with a LeCroy WaveRunner 44Xi oscilloscope. Thus both acetone fluorescence and ethylene Rayleigh scattering were captured with the same CCD camera, and no additional overlap of images was necessary. Peak quantum efficiency of the camera is about 50 %, while read noise is specified to be 11 e$^-$ at 10 Msamples s^{-1} readout rate (using two ADCs). Signals are digitized to 14-bit resolution. A second PCO camera was used to record the reference acetone image.

Background images were acquired using helium as the scattering gas (with no acetone); background scattering was strongly suppressed using a series of baffles

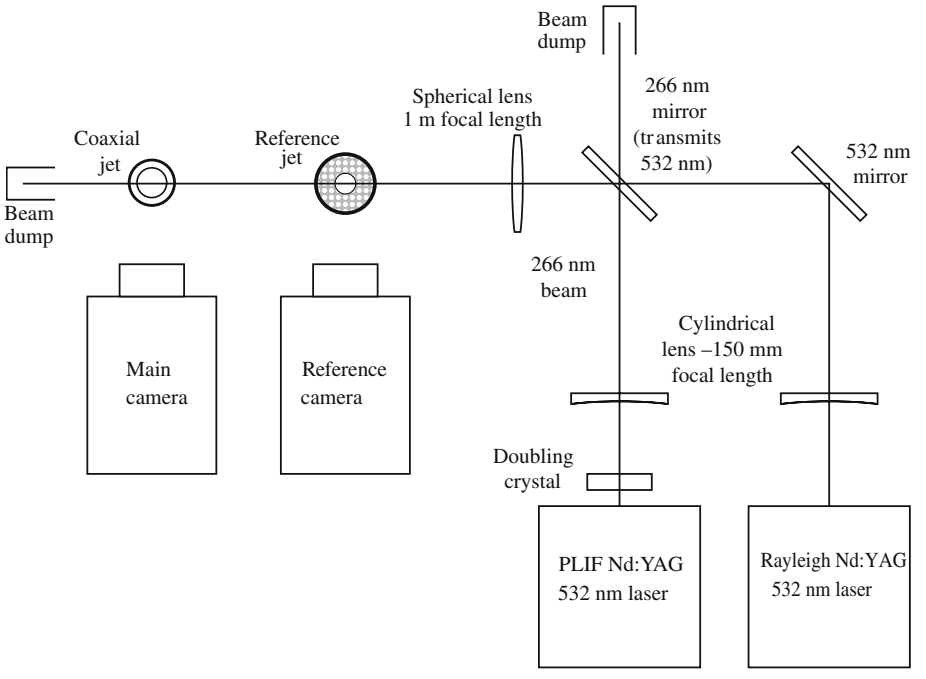

FIGURE 2. Schematic of the experimental setup.

and enclosing the entire flowpath and collection system. Images were normalized with an average image derived from uniform fields of Rayleigh scattering or acetone fluorescence. This normalization procedure accounted for inherent image non-uniformity and for the laser fluence distribution. The reference jet was set up along the laser sheet path right before the main flow field. Acetone PLIF images from the reference flow were then recorded for each image, allowing a quantification of the relative acetone concentration for each image.

The PCO-1600 camera was equipped with a custom lens arrangement consisting of a 200 mm focal length Rodenstock lens followed by 58 mm focal length, $f/1.2$ Nikon Noct-Nikkor lens. The Rodenstock lens was placed such that it was at its focal length (200 mm) from the target while the Nikon lens was then operated at infinity. The lenses were butted up against one another. The scalar image pixel size for the camera is 55 μm. The actual image resolution, which also includes the optical blurring, was quantified by translating a razor blade across the image plane and deriving the line-spread function (Wang & Clemens 2004). The full width at half maximum (FWHM) of the line-spread function is ≈76 μm. We estimated the Kolmogorov scale (63 μm) on the centreline of the flow exiting the centre tube by extrapolating the measurement results given in Bailey *et al.* (2009). The Kolmogorov scale of the annular exit flow was estimated using channel flow data (Antonia *et al.* 1992; Lavertu & Mydlarski 2005), as the radius ratio for the annulus is large (≈0.758). At the mid-point radial location, the estimated value is 13 μm. This Kolmogorov scale is smaller than the FWHM of the imaging system. Scalar fluctuations, however, are generated due to the mixing of the streams. At these near-field locations, the scalar dissipation length scales are difficult to estimate, and hence also the required spatial resolution. Instead, we estimated the extent to which the scalar dissipation rates are resolved using a

conditional sampling-based method for noise correction and resolution estimation (Cai & Tong 2009; Cai *et al.* 2010). It was determined that the dissipation rates were 98 % or better resolved.

The laser sheets were aligned with the central chord of the jet, which itself was located in the centre of the 150 mm diameter air co-flow. This entire three-stream flow system was mounted on a large three-axis translation system equipped with optical encoders. Thus, the flow field could be translated to any downstream position with high accuracy. The downstream image location for the first measurement station was quantified by imaging a ruler placed on the annular jet.

2.2. *Data reduction and analysis procedure*

The PLIF and Rayleigh scattering images were processed to remove the background and camera offset, and to normalize the beam profiles. The camera offsets were obtained with the camera lens closed. The laser profile variations for the 266 nm beam were corrected using the reference camera. The variations for the 532 nm beam were corrected using scattering from the co-flow air. A target grid was imaged to remove any optical distortion.

Acetone PLIF and Rayleigh scattering images were used to obtain the mole fractions of the two streams. The PLIF signal, S_P, from acetone is far from saturated; therefore, it is a linear function of incident laser pulse energy (Taylor 1993)

$$S_P(x, y) = R_P(x, y)I_P(x, y)\sigma_P C X_1(x, y) Y(x, y) + B_P(x, y), \tag{2.1}$$

where R_P, I_P, σ_P, C, X_1, Y and B_P are the camera response, the laser pulse energy, the acetone cross-section, the mole fraction of acetone in acetone-doped air, the mole fraction of the acetone-doped air, the acetone fluorescence yield and the background signal, respectively. The fluorescence yields of acetone fluorescence with ethylene versus air are corrected using a ratio of 0.775. This was quantified in an experiment in which 1 SLPM of air was sent through the acetone bubbler (and the resulting acetone flow was $\approx$1.4 SLPM); 35 SLPM of either air or ethylene was then combined with this flow and the difference in fluorescence yield was measured. The effect on the fluorescence yield due to acetone itself was quantified and was determined to be negligible. The Rayleigh signal S_R has a similar functional form (Taylor 1993),

$$S_R(x, y) = R_R(x, y)I_R(x, y)\sigma_{eff} + B_R(x, y), \tag{2.2}$$

where R_R, I_R, B_R and σ_{eff} are the camera response to the Rayleigh signal, the laser pulse energy, the background signal and the effective Rayleigh cross-section, respectively. The effective Rayleigh cross-section is the mole-weighted average of Rayleigh cross-section of each species

$$\sigma_{eff} = \sigma_1 X_1 + \sigma_2 X_2 + \sigma_3 X_3, \tag{2.3}$$

where σ_i values are the corresponding Rayleigh cross-section, and X_i values are the mole fractions of each stream and satisfy the relation

$$X_1 + X_2 + X_3 = 1. \tag{2.4}$$

Beam attenuation due to acetone absorption is also accounted for. The acetone absorption coefficient was determined by fitting the fluorescence signal with Beer's law. Sample images of the acetone-doped air (centre jet) and ethylene (annular flow) are shown in figure 3.

To improve the statistical convergence, the mean scalar dissipation rates and the cross-dissipation rate were averaged over 3 pixels and 5 pixels in the radial and axial

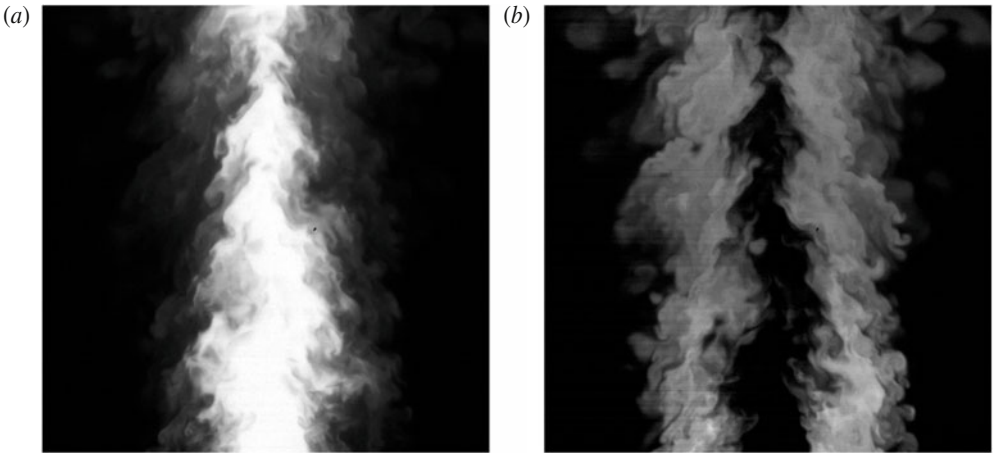

FIGURE 3. Sample images of the centre jet stream (*a*) and the annular flow (*b*). The bottom and the top of the images are located at $x/d = 3.21$ and 7.17 respectively.

Derivative order	b_1	b_2	b_3	b_4	b_5
1st	2100/2520	−600/2520	150/2520	−25/2520	2/2520
2nd	42 000/25 200	−6000/25 200	1000/25 200	−125/25 200	8/25200

TABLE 2. 10th-order central finite difference schemes for first and second derivatives.

directions (0.165 and 0.275 mm) respectively. Conditional statistics were averaged over 5 pixels and 9 pixels in these directions (0.275 and 0.495 mm) respectively. Conditional means and PDFs were calculated using Kernel Density Estimation (KDE) (Wand & Jones 1995) in two dimensions with a resolution of 400 × 400 in the sample space and an oversmooth parameter of 1.3. Noise correction was applied to the mean and conditional scalar dissipation, scalar variances and scalar correlation coefficient using a new method developed by Cai & Tong (2009). The scalar dissipation and diffusion were obtained using scalar derivatives in the measurement plane (two components), which were computed using the 10th-order central difference scheme shown in (2.5) and (2.6):

$$h\,u' = b_1(u_1 - u_{-1}) + b_2(u_2 - u_{-2}) + b_3(u_3 - u_{-3}) + \cdots, \tag{2.5}$$

$$h^2u'' = b_1(u_{-1} - 2u_0 + u_1) + b_2(u_{-2} - 2u_0 + u_2) + b_3(u_{-3} - 2u_0 + u_3) + \cdots. \tag{2.6}$$

The coefficients are listed in table 2. The diffusion coefficient, D, is 0.1039 cm^2 s^{-1} for acetone (at 20 °C) and 0.1469 cm^2 s^{-1} for ethylene (Reid, Prausnitz & Poling 1989).

3. Results

In this section the scalar means, variances, dissipation time scales, correlation coefficient, segregation parameter, mean and conditional dissipation rates, and conditional scalar diffusion computed from the two-dimensional images were analysed to study the mixing process. Typically 3000–5400 images were used to obtain the statistics. Noise correction and the resolution estimation were performed for variances,

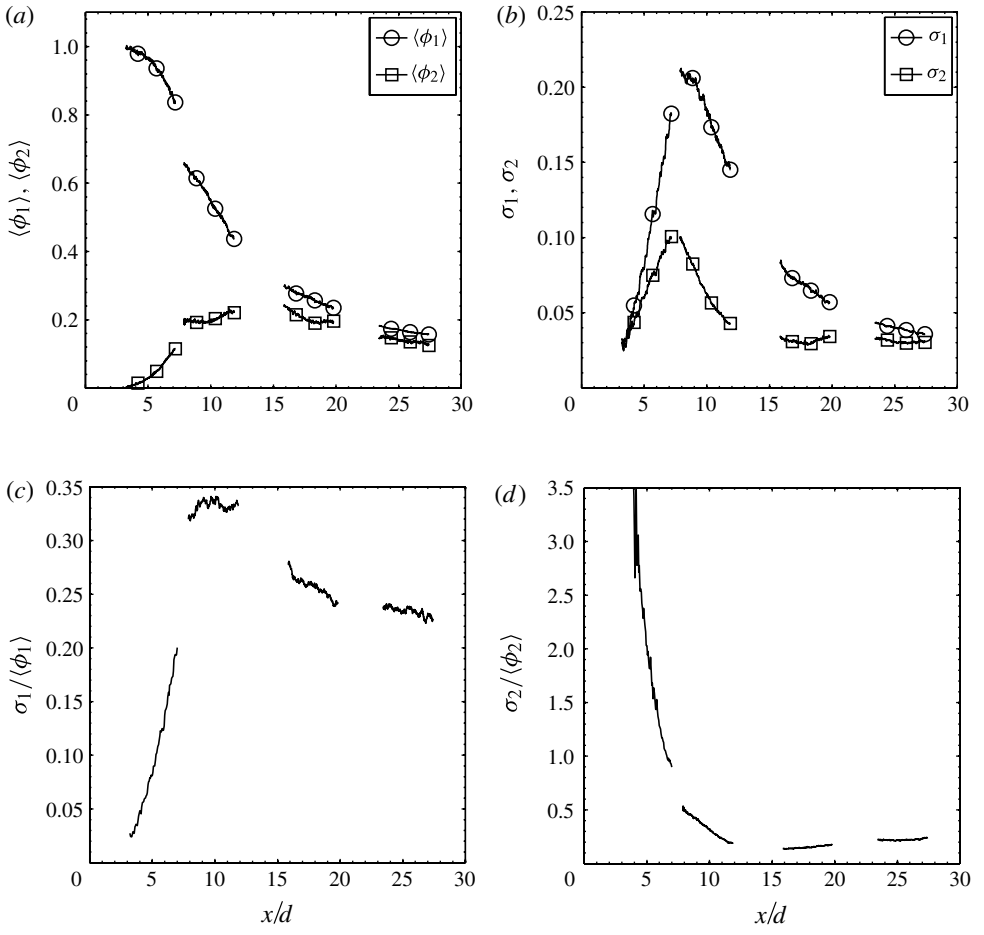

FIGURE 4. Evolution of the mean scalar, the r.m.s. scalar fluctuations and the fluctuation intensities along the jet centreline.

correlation coefficient, segregation parameter, mean dissipation rates, and conditional dissipation rates. We find that the resolution combined with the 10th-order explicit finite difference scheme are capable of resolving the scalar dissipation rate. Details of the method and procedures are given in Appendix A and in Cai & Tong (2009). An analysis of the uncertainties of the statistics was performed and is given in Appendix B.

3.1. *Evolution along the jet centreline*

The mean scalar and r.m.s. profiles along the jet centreline are shown in figure 4(*a*). Very close to the jet exit ($x/d < 4$, where d is the diameter of the centre jet tube) there is essentially only ϕ_1 on the jet centreline. Downstream of this location ϕ_2 begins to reach the centreline, and $\langle\phi_1\rangle$ begins to decrease. For $x/d < 7$ there is essentially no co-flow air on the centreline, i.e. $\phi_1 + \phi_2 \approx 1$. Further downstream, co-flow air as well as more ϕ_2 reach the centreline, and $\langle\phi_1\rangle$ decreases monotonically. At the same time, $\langle\phi_2\rangle$ increases and reaches a maximum at $\approx x/d = 12$. Downstream of this location, $\langle\phi_2\rangle$ decreases along with $\langle\phi_1\rangle$ as more co-flow air reaches the centreline. By $x/d = 25$,

the mean values for the two scalars appear to be proportional to each other, suggesting that the two scalars are quite well mixed and their mixture is mixing largely in unison with the co-flow air; therefore, the mixing problem becomes similar to two-stream mixing further downstream.

For both scalars, the r.m.s. fluctuations, $\sigma_1 = \langle \phi_1'^2 \rangle$, $\sigma_2 = \langle \phi_2'^2 \rangle$, are small very close to the jet exit (figure 4*b*), where ϕ_1' and ϕ_2' are the scalar fluctuations. The r.m.s. fluctuations become significant near $x/d = 4$ and reach the maximum values near $x/d = 7.5$. The maximum fluctuations for ϕ_1 are almost three times those of ϕ_2. Again, by $x/d = 25$ the r.m.s. values for the two scalars appear to be proportional to each other.

The fluctuation intensities on the jet centreline for the scalars, $\sigma_1/\langle \phi_1 \rangle$ and $\sigma_2/\langle \phi_2 \rangle$, are also shown in figure 4. Near the jet exit $\sigma_1/\langle \phi_1 \rangle$ is small due to the low fluctuations. It rises rapidly with x/d due to the rapid increase of σ_1, and reaches the maximum near $x/d = 10$. Further downstream it appears to approach an asymptotic value of $\approx$0.21, the value in the self-similar region of binary jet mixing (e.g. Dowling & Dimotakis 1990; Tong & Warhaft 1995), indicating that ϕ_1 is well mixed. The value of $\sigma_2/\langle \phi_2 \rangle$ is large near the jet exit due to the extremely low values of $\langle \phi_2 \rangle$. Moving downstream it drops rapidly due to the rapid increase of $\langle \phi_2 \rangle$, and also appears to approach the asymptotic values of 0.21, again indicating that ϕ_2 is well mixed. The trend of $\sigma_2/\langle \phi_2 \rangle$ is similar to that of temperature fluctuations produced by a heated ring placed in a turbulent jet (Tong & Warhaft 1995). These results show that in the near field the evolution processes of the two scalars are distinctively different, while far downstream they may be similar.

The mean and r.m.s. values of the two scalars are measures of the evolution of the individual scalar fields, but not of the extent of mixing among the three scalars. The correlation coefficient between the scalar fluctuations provides an effective way to characterize the extent of mixing. The correlation coefficient, $\rho = \langle \phi_1' \phi_2' \rangle / (\sigma_1 \sigma_2)$, between ϕ_1 and ϕ_2 would equal negative one in the absence of the co-flow air at the measurement location, regardless of the state of mixing between ϕ_1 and ϕ_2, because when $\phi_1 + \phi_2 = 1$ (no co-flow air), their fluctuations are anti-correlated with equal magnitudes. Positive correlation, on the other hand, would indicate mixing of the two scalars at the molecular level and presence of co-flow air at the measurement location, but mixing of air with ϕ_1 and ϕ_2 is not necessary. The correlation coefficient (figure 5*a*) for $x/d < 7$ is close to negative one, indicating absence of co-flow air in this part of the centreline. For $x/d > 7$ the correlation begins to increase, indicating mixing between ϕ_1 and ϕ_2 and the presence of co-flow air. For $x/d > 20$, ϕ_1 and ϕ_2 are well mixed, and their mixture is mixing with co-flow air, reflected by a correlation coefficient close to unity. Several previous studies (Warhaft 1981, 1984; Tong & Warhaft 1995) also show that the correlation coefficient increases from -1 to 1.

Another measure of the extent of mixing between ϕ_1 and ϕ_2 is the segregation parameter α, defined as $\langle \phi_1' \phi_2' \rangle / (\langle \phi_1 \rangle \langle \phi_2 \rangle)$, or $\langle \phi_1 \phi_2 \rangle = \langle \phi_1 \rangle \langle \phi_2 \rangle (1 + \alpha)$ (e.g. Komori *et al.* 1991; Tong & Warhaft 1995). When there is no mixing between ϕ_1 and ϕ_2, i.e. $\langle \phi_1 \phi_2 \rangle = 0$, $\alpha = -1$. The evolution of α on the jet centreline is shown in figure 5(*b*). For $x/d < 4$, $\langle \phi_2 \rangle$ has very low values ($<$0.02) and the measurements are less accurate, resulting in a large error in α. Thus, we only plot the α values for $x/d > 4$. Nevertheless, an asymptotic value of α for $x/d \to 0$ can be inferred. Here $\rho \approx -1$, $\langle \phi_1 \rangle \approx 1$, $\sigma_1 \approx \sigma_2$ (no air, mixing between ϕ_1 and ϕ_2 only), and α can be

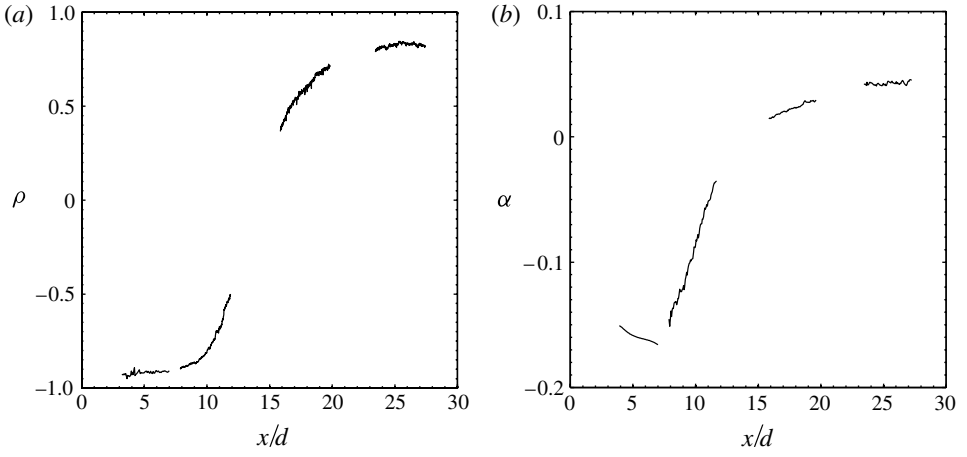

FIGURE 5. Evolution of the correlation coefficient and segregation parameter between ϕ_1 and ϕ_2 on the jet centreline.

approximated as

$$\alpha \approx -\frac{\langle \phi_2^2 \rangle - \langle \phi_2 \rangle^2}{\langle \phi_2 \rangle} = -\left\{ \frac{\int P_2 \hat{\phi}_2^2 \, \mathrm{d}\hat{\phi}_2}{\int P_2 \hat{\phi}_2 \, \mathrm{d}\hat{\phi}_2} - \int P_2 \hat{\phi}_2 \, \mathrm{d}\hat{\phi}_2 \right\}, \tag{3.1}$$

where P_2 is the marginal PDF of ϕ_2. As $x/d \to 0$, $P_2(\hat{\phi}_2)$ is increasingly concentrated near $\hat{\phi}_2 = 0$. Thus, $\langle \phi_2 \rangle \approx 0$ and $\int P_2 \hat{\phi}_2^2 \, \mathrm{d}\hat{\phi}_2 \ll \int P_2 \hat{\phi}_2 \, \mathrm{d}\hat{\phi}_2$, since $P_2 \hat{\phi}_2^2 \ll P_2 \hat{\phi}_2$, resulting in $\alpha \approx 0$. As x/d increases, mixing between ϕ_1 and ϕ_2 causes $\langle \phi_1' \phi_2' \rangle$ to become negative and to increase in magnitude, and α becomes negative, reaching the largest negative value near $x/d = 7$. Further downstream $\langle \phi_2 \rangle$ grows, resulting in smaller α magnitudes. Far downstream $\rho \to 1$, $\alpha = \sigma_1 \sigma_2 / (\langle \phi_1 \rangle \langle \phi_2 \rangle)$ will approach an asymptotic value ($\approx$0.045) as $\sigma_1 / \langle \phi_1 \rangle$ and $\sigma_2 / \langle \phi_2 \rangle$ approach asymptotic values. This trend of evolution is similar to that found by Komori *et al.* (1991), although the behaviour at small times (equivalent to $x/d \to 0$) was not given in that work.

Figure 6 shows the evolution of the scalar JPDF of ϕ_1 and ϕ_2 along the jet centreline. We use greyscale and isocontours to represent the JPDF values. The outermost contour represents the boundary within which the JPDF integrates to 99 %. The JPDF should be confined to a triangle in the ϕ_1–ϕ_2 space with the vertices at (0, 0), (0, 1) and (1, 0), where the co-ordinates denote the sample-space variables for ϕ_1 and ϕ_2, respectively. At $x/d = 3.29$ the JPDF is largely concentrated near (1, 0) in the scalar space. At $x/d = 4.01$ the JPDF begins to extend towards (0, 1), i.e. the ϕ_2 side, indicating that ϕ_2 begins to mix with ϕ_1. At these locations there is essentially no co-flow air. The JPDF should be on the mixing line connecting (0, 1) and (1, 0); however, figure 6 shows that the JPDF extends beyond the boundary of the allowed scalar space largely due to measurement noise. In general, the measured JPDF is broadened by the measurement noise. In some cases, the outermost contour (99 % probability) is primarily noise-related (e.g. JPDF at $r/d = 0.387$ and $x/d = 6.99$ in figure 17), but in other cases the contour also contains real scalar fluctuations. As a result, we choose to include this contour in all JPDF figures.

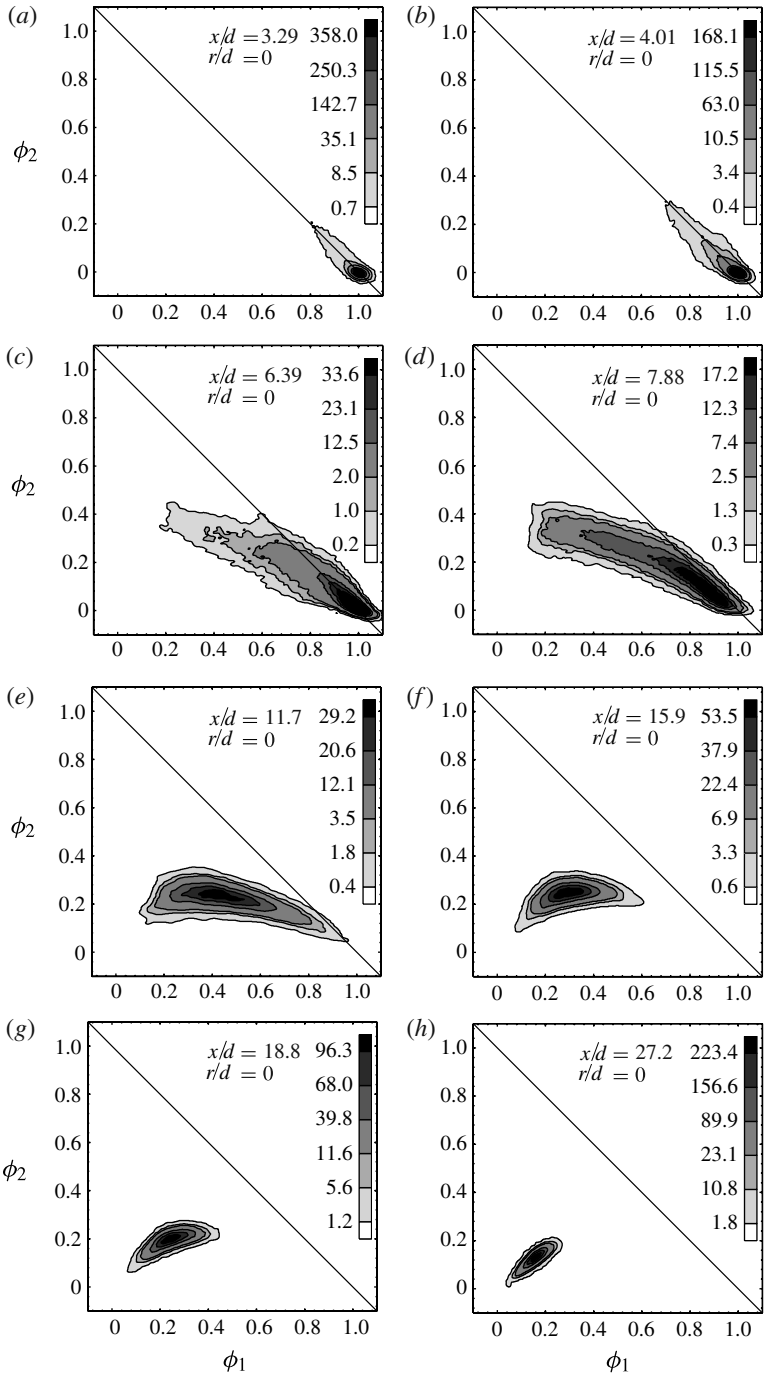

FIGURE 6. Evolution of the scalar JPDF on the jet centreline. The downstream location is listed in the top of each figure. The last three contours correspond to boundaries within which the JPDF integrates to 90 %, 95 % and 99 %, respectively, throughout the paper. The rest of the contours scale linearly over the remaining range.

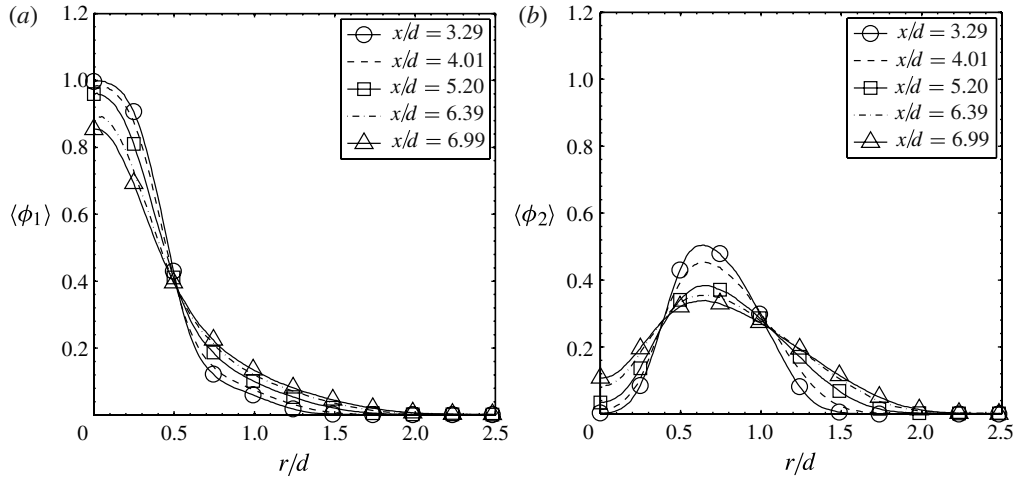

FIGURE 7. Cross-stream profiles of the mean scalars. The downstream locations are given in the legend.

As the downstream distance further increases to $x/d = 6.39$, the JPDF extends further towards $(0, 1)$ and some air is present on the centreline, bending the tail of the JPDF towards $(0, 0)$. The 'ridgeline' of the JPDF still has a negative slope in the scalar space, consistent with the negative correlation between ϕ_1 and ϕ_2. Further downstream, the bending of the JPDF continues. At $x/d = 7.88$, the JPDF reaches $(0.15, 0.3)$, indicating the presence of mixtures with little ϕ_1. The JPDF peak is still near $(1, 0)$. At $x/d = 11.7$, the JPDF is almost horizontal, consistent with the smaller correlation coefficient. The JPDF peak shifts to the centre part of the JPDF, indicating more complete mixing. Beyond $x/d = 15.9$, the ridgeline of JPDF has a positive slope and the correlation becomes positive. At $x/d = 27.2$, ϕ_1 and ϕ_2 are limited largely to within 0.2 and 0.3, respectively, and are largely proportional to each other, indicating that the two scalars are well mixed. Their mixture (also containing some air) is being mixed with co-flow air, resulting in positive correlation.

The above results along the jet centreline show that the most unique and interesting part of the present three-scalar mixing is the near field, on which we focus the rest of the discussions. We first discuss the radial profiles of the scalar means, variances, correlation, and dissipation rates. Then we discuss the scalar JPDF, the conditional scalar diffusion and the conditional scalar dissipation rates.

3.2. *Cross-stream profiles*

The radial profiles of the mean scalars are shown in figure 7. The profiles of $\langle\phi_1\rangle$ have Gaussian-like shapes. For these downstream locations the half-width points (the location where $\langle\phi_1\rangle$ is one half of its maximum value) are at $\approx r/d = 0.5$. Moving downstream, the profiles extend to larger r/d values as the jet spreads. The mean profiles of $\langle\phi_2\rangle$ have off-centreline peaks, with the peak positions at $\approx r/d = 0.65$.

The profile of the r.m.s. fluctuations of ϕ_1 at each downstream location have an off-centreline peak (figure 8*a*). The peak position is close to $r/d = 0.5$ and moves slightly towards the centreline as x/d increases. This shift coincides with the slight shift of the location of the maximum mean scalar gradient for each profile (not shown) at which the production of the variance is likely to be largest. On the centreline there

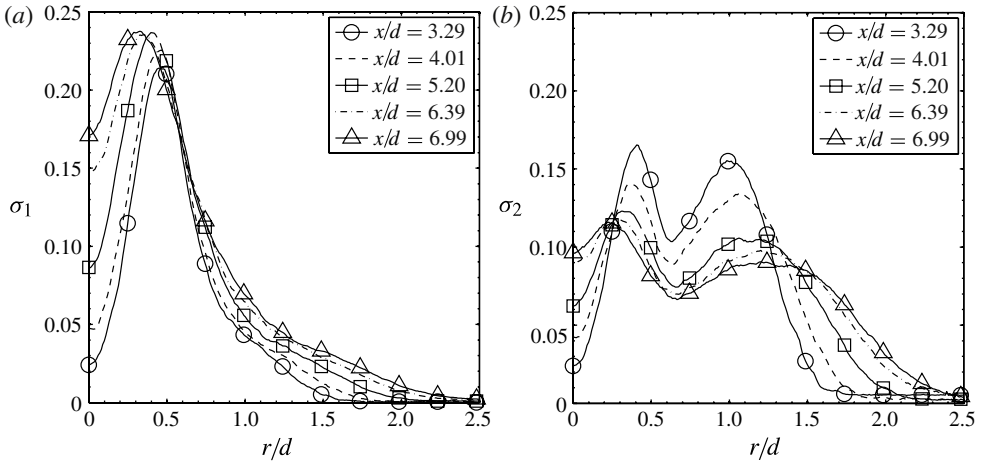

FIGURE 8. Corrected cross-stream profiles of the r.m.s. scalar fluctuations. The downstream locations are given in the legend.

is no production of the variance; therefore, mean advection and turbulent transport are responsible for the non-zero r.m.s. values. The maximum r.m.s. values are ≈25 % of the maximum mean values.

Each r.m.s. profile for ϕ_2 has two off-centreline peaks (figure 8*b*), one on each side of the maximum of the mean profile, reflecting the dominant role of the production of the scalar variance, which has maximum values near the peak mean gradient. The minimum point between the peaks is approximately at the location of the maximum of the mean profile. There is no production of the variance at this location and on the centreline; therefore, mean advection and turbulent transport again are responsible for the non-zero r.m.s. values. The maximum r.m.s. values are ≈30 % of the maximum mean values, higher than the percentage for ϕ_1.

The radial profiles of the fluctuation intensity are shown in figure 9. Up to $x/d = 6.39$, $\sigma_1/\langle\phi_1\rangle$ largely increase with r/d, only dipping slightly near $r/d = 0.8$. Further downstream, it increases monotonically with r/d, appearing to flatten out beyond $r/d = 0.6$. The profiles of $\sigma_2/\langle\phi_2\rangle$ generally have a minimum point near $r/d = 0.7$. The values for small and large r/d decreases with increasing downstream location, reflecting the progression of the mixing process.

The cross-stream profiles of the correlation coefficient (figure 10*a*) between ϕ_1 and ϕ_2 from $x/d = 3.29$ to 6.99 show a similar trend. For $r/d < 0.4$, there is little air present. The mixing is largely binary (between ϕ_1 and ϕ_2), resulting in an almost perfect anti-correlation ($\rho = -1$). The deviation of ρ from -1 near the centreline is due to measurement noise. As r/d increases, there is more air as well as more mixing between ϕ_1 and ϕ_2, and the correlation begins to increase. Beyond $r/d = 1$, the ϕ_1 and ϕ_2 values are very low most of the time. Higher values occur when fluid carrying mixed ϕ_1 and ϕ_2 from the inner part of the flow is advected to the measurement location by large flow structures. This process produces similar structures in both ϕ_1 and ϕ_2 fields, resulting in a positive correlation. The correlation coefficient approaches unity for large r/d.

The cross-stream profiles of α are shown in figure 10. The profiles generally have a minimum near $r/d = 0.2$, increasing slightly toward the centreline (the profile at $x/d = 3.29$ is only given for $r/d > 0.2$ as it cannot be accurately measured

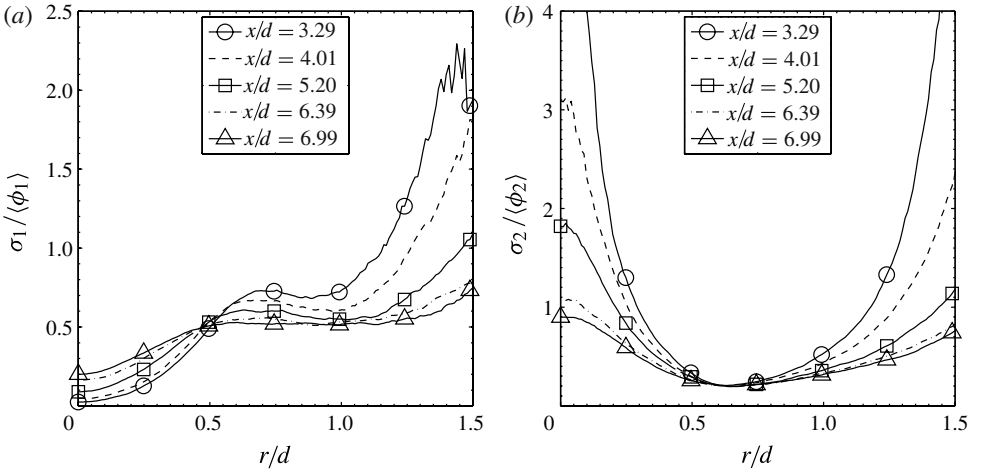

FIGURE 9. Corrected cross-stream profiles of the fluctuation intensities. The downstream locations are given in the legend.

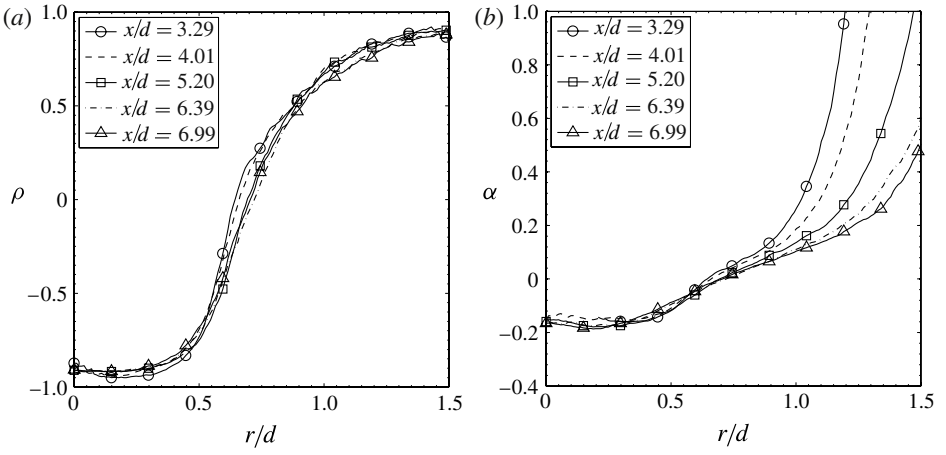

FIGURE 10. Corrected cross-stream profiles of the scalar correlation coefficient and segregation parameter. The downstream locations are given in the legend.

for $r/d < 0.2$). For large r/d, α becomes positive, due to the positive correlation and higher scalar fluctuation intensities.

The cross-stream profiles of the mean scalar dissipation rates are shown in figure 11. The dissipation rate for ϕ_1, $\langle\chi_1\rangle$, at $x/d = 3.29$ peaks near $r/d = 0.44$, the same location for the peak of the r.m.s. fluctuations. On the jet centreline there is essentially no dissipation because there are little scalar fluctuations. As x/d increases $\langle\chi_1\rangle$ increases on the centreline. The peak dissipation rate decreases and the location of the peak shifts slightly towards the centreline. If the time scale for the spectral transfer of the scalar variance is constant across the jet, and if there is no turbulent transport for the dissipation rate, the dissipation rate profiles can be expected to be similar to the scalar variance profiles. At $x/d = 6.99$ the ratio of the peak dissipation to the centreline dissipation is $\approx$1.6, smaller than the ratio of the peak to centreline

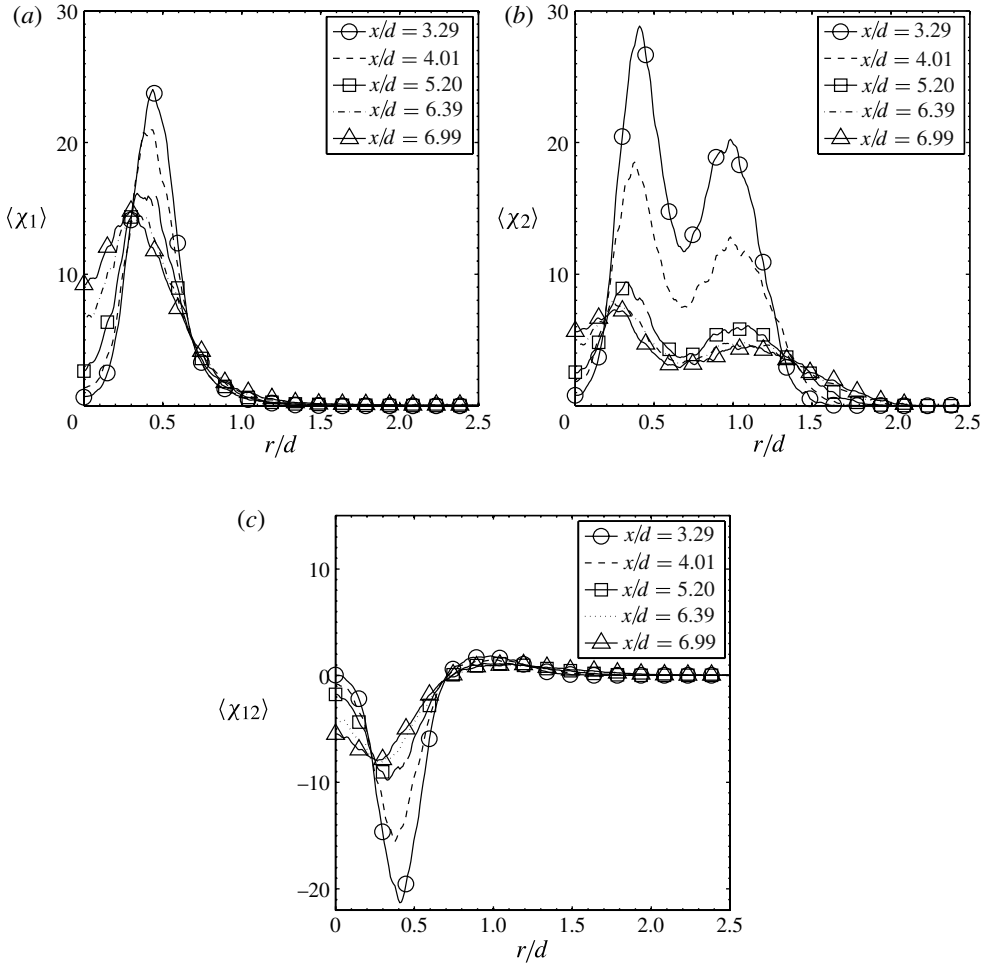

FIGURE 11. Corrected cross-stream profiles of the mean scalar dissipation rates and the mean cross-dissipation rate.

variances (≈1.9), suggesting that the time scale for the spectral transfer varies across the jet. In addition, turbulent transport also plays an important role in the dissipation rate budget.

The mean dissipation rate for ϕ_2, $\langle\chi_2\rangle$, has two peaks at $r/d = 3.29$, similar to the r.m.s. fluctuations, but the outer peak is not as strong as that of the r.m.s. fluctuations. As x/d increases the inner peak shifts towards the centreline and the outer one away from it. At $r/d = 6.99$ the ratios of the inner peak dissipation to the centreline dissipation is ≈1.3, comparable to the ratio of the peak to centreline variances (≈1.3). The ratio of the values of the two dissipation peaks (≈1.59) is smaller than the ratio of the two peak scalar variance values (≈1.64), indicating that there are some cross-stream variations in the time scale of spectral transfer.

The cross-stream profiles of the mean cross-dissipation between ϕ_1 and ϕ_2, defined as $\langle\chi_{12}\rangle = \langle 2D(\partial\phi_1/\partial x_i)(\partial\phi_2/\partial x_i)\rangle$, are shown in figure 11(*c*), where D is the average diffusivity of acetone and ethylene. The cross-dissipation generally has a small negative value on the jet centreline. Away from the centreline, the magnitude

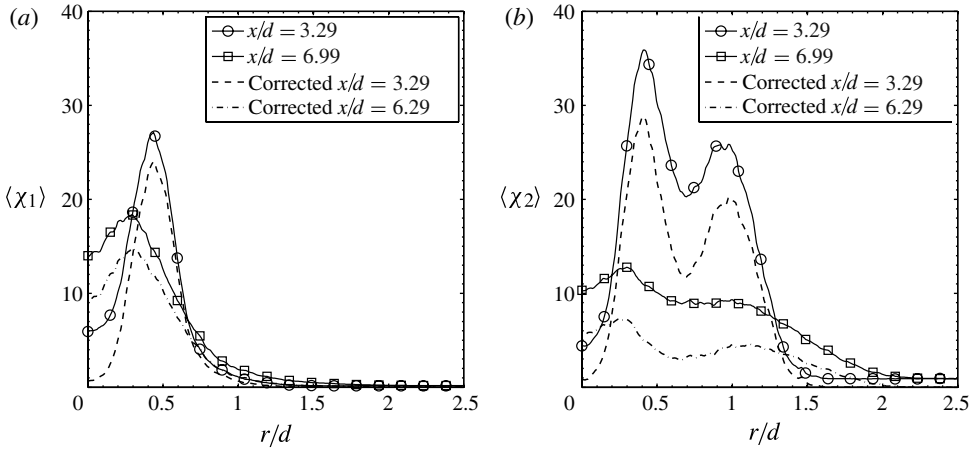

FIGURE 12. Cross-stream profiles of the mean scalar dissipation rate with and without noise correction. The downstream locations are given in the legend.

increases, reaching a maximum before decreasing. It appears to overshoot slightly to positive values before approaching zero at large r/d. The negative peak shifts from $r/d = 0.4$ at $x/d = 3.29$ to $r/d = 0.3$ at $x/d = 6.99$, approximately coinciding with the location of the peak of $\langle\chi_1\rangle$ and the inner peak of $\langle\chi_2\rangle$. At these radial locations, mixing is primarily between ϕ_1 and ϕ_2, as reflected by the values (≈ -1) of the correlation coefficient; therefore, their small-scale fluctuations are anti-correlated, resulting in negative $\langle\chi_{12}\rangle$. One can define a vectorial correlation coefficient, $(2D\langle\nabla\phi_1 \cdot \nabla\phi_2\rangle)/(\langle\chi_1\rangle\langle\chi_2\rangle)^{1/2}$, as a measure of the relationship between $\nabla\phi_1$ and $\nabla\phi_2$. At $r/d = 0.4$ at $x/d = 3.29$, where $\langle\chi_{12}\rangle$ peaks, the value is ≈ -0.81, indicating a high degree of anti-correlation between $\nabla\phi_1$ and $\nabla\phi_2$, in both direction and magnitude. The high negative correlation remains at the peak location at $x/d = 6.99$. Tong & Warhaft (1995) measured the coherency spectrum of two scalars, which is a measure of the correlation coefficient as a function of scale (or wavenumber). They showed that the dissipation scale fluctuations are negatively correlated in the near field, consistent with the present results on $\langle\chi_{12}\rangle$.

The dissipation rate measurements are affected by the measurement noise. Figure 12 compares the values of $\langle\chi_1\rangle$ and $\langle\chi_2\rangle$ before and after noise correction for two downstream locations ($x/d = 3.29$ and 6.99). The amounts of correction are generally large near the peak mean scalar values. The details of the noise correction method is given in Appendix A.

The scalar dissipation time scale, defined as $\langle\phi'^2\rangle/\langle\chi\rangle$, represents the time scale at which fractional changes (dissipation) of scalar variance occur. At $x/d = 3.29$ and 4.01, the time scales generally are smaller on the jet centreline and increase away from it (figure 13). Further downstream $\langle\phi_1'^2\rangle/\langle\chi_1\rangle$ has a mild peak near $r/d = 0.4$, whereas $\langle\phi_2'^2\rangle/\langle\chi_2\rangle$ peaks near $r/d = 0.3$. The peak values of the dissipation time scale for ϕ_1 are generally larger than those for ϕ_2 by approximately a factor of two, perhaps partly reflecting the mean velocity difference between the ϕ_2 stream and the co-flow air. In addition the radial dimension of the annulus is smaller than the centre jet tube diameter, which also tends to increases the rate of mixing and reduce the dissipation time scale.

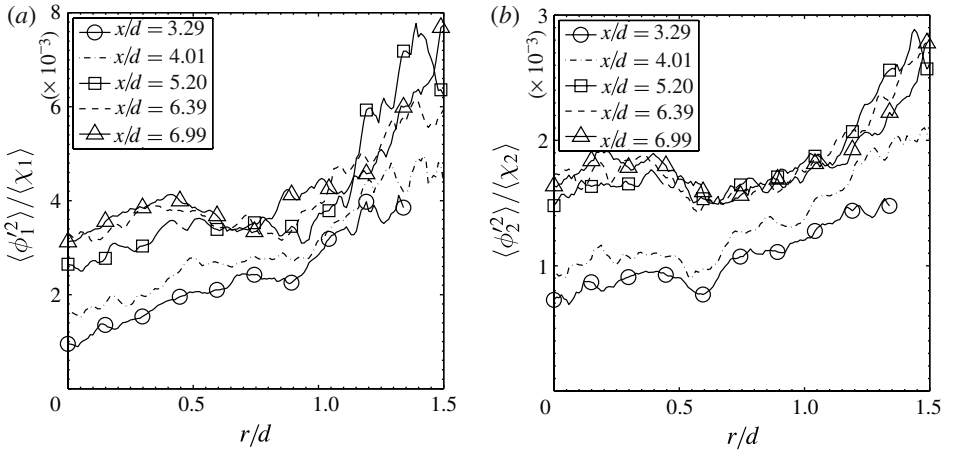

FIGURE 13. Corrected cross-stream profiles of the scalar dissipation time scales.

3.3. *JPDF, conditional diffusion, and conditional dissipation*

In this subsection we discuss in detail the scalar JPDF, the conditional diffusion, the conditional dissipation rates, and the conditional cross-dissipation rate for ϕ_1 and ϕ_2 at two downstream locations ($x/d = 3.29$ and 6.99). The scalar diffusion evolves the scalar JPDF through the mean scalar diffusion conditional on the two scalars, $\langle D\nabla^2\phi_1 \mid \phi_1, \phi_2\rangle$ and $\langle D\nabla^2\phi_2 \mid \phi_1, \phi_2\rangle$. The diffusion terms in the JPDF equation transport the JPDF in the scalar space; therefore, the conditional diffusion represents the two components of a diffusion (or transport) velocity. We present the conditional diffusion as the diffusion velocity, represented by streamlines and magnitudes (using isocontours). An analysis of the JPDF equation suggests that both conditional diffusion terms can be normalized by the dissipation time scale for ϕ_1. Because both scalars are normalized at the jet exit, there is no need to normalize the sample-space variable for the scalars.

The results for $x/d = 3.29$ at three radial locations are shown in figures 14 and 15. On the centreline, the mixture is essentially pure ϕ_1 (figure 6). At $r/d = 0.149$ (not shown), the JPDF begins to extend towards $(0, 1)$ along the straight (mixing) line connecting $(0, 1)$ and $(1, 0)$, indicating that there is some ϕ_2 mixed with ϕ_1 but there is no co-flow air.

At $r/d = 0.347$, the JPDF extends further towards $(0, 1)$, a larger amount of ϕ_2. There is also some co-flow air in the mixture as indicated by the JPDF near $(0.2, 0.5)$. The composition near $(0.2, 0.5)$ comes from the air side, containing both ϕ_2 and air. The JPDF near the ϕ_1–ϕ_2 mixing line is about twice as wide as that on the jet centreline, indicating that turbulent mixing begins to dominate the broadening of the JPDF. The diffusion streamlines generally move towards the mixing line. A manifold begins to emerge near $(0.3, 0.5)$, towards which the diffusion streamlines first converge. The mean composition, $(\langle\phi_1\rangle, \langle\phi_2\rangle)$, is indicated by a solid circle in the streamline plot.

Moving further away from the jet centreline the JPDF extends further towards $(0, 1)$, and then bends down towards $(0, 0)$, indicating that there is more air in the mixture. At $r/d = 0.536$, which is near the $\langle\phi_2\rangle$ peak, the JPDF becomes bimodal, with two peaks near $(0.10, 0.50)$ and $(0.4, 0.5)$, representing mostly ϕ_2–air and ϕ_1–ϕ_2 mixtures, respectively. The JPDF peaks are a result of flapping of the two mixtures by the

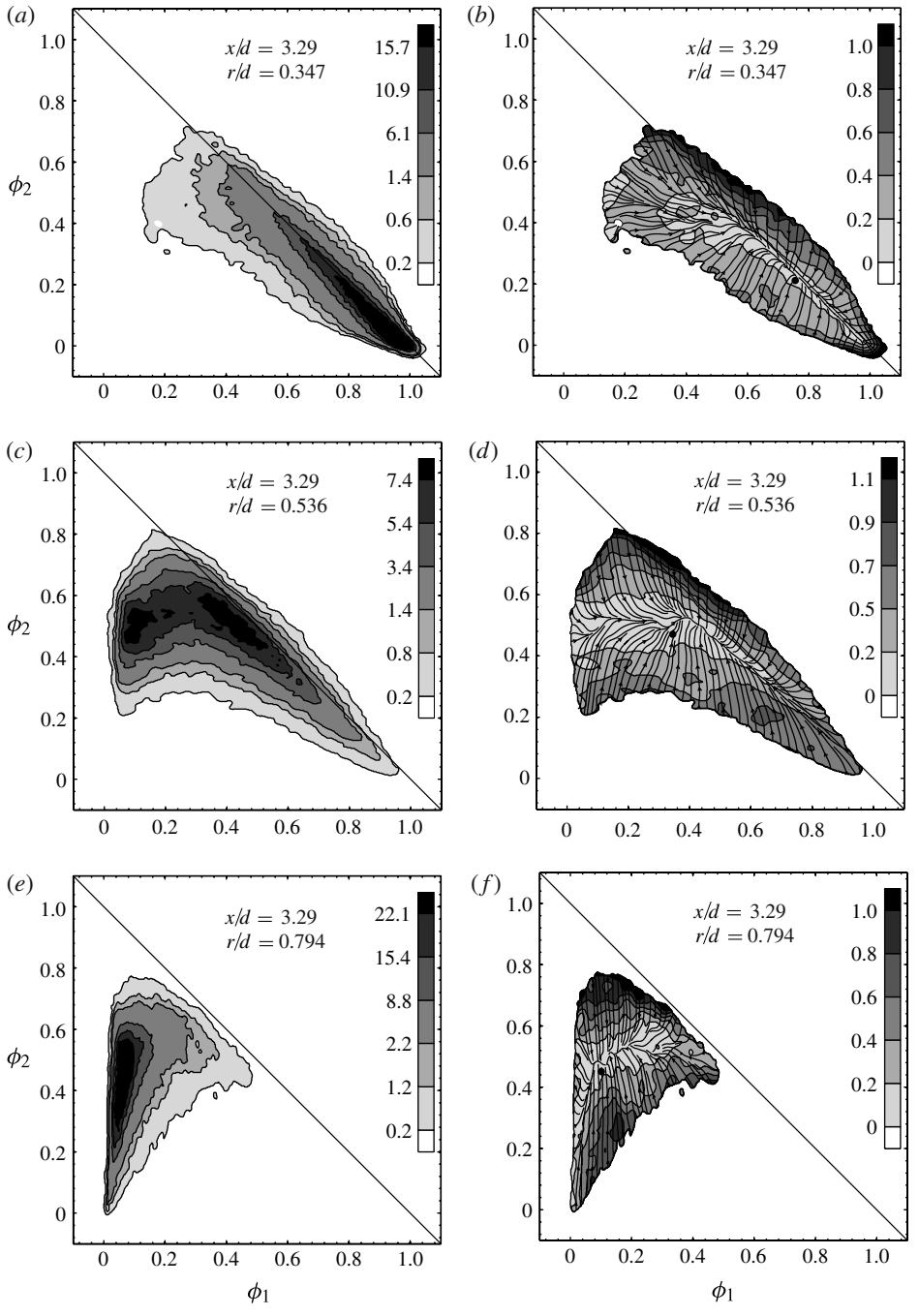

FIGURE 14. The cross-stream evolution of the scalar JPDF (*a,c,e*) and the corresponding conditional diffusion (*b,d,f*) at $x/d = 3.29$. The radial location is given at the top of each figure. The last three JPDF contours correspond to the same integrated probabilities given in figure 6. The contour magnitudes of the diffusion are the Euclidean norm of the diffusion velocity vector. The mean scalars ($\langle\phi_1\rangle$, $\langle\phi_2\rangle$) are indicated in each streamline plot by a solid circle.

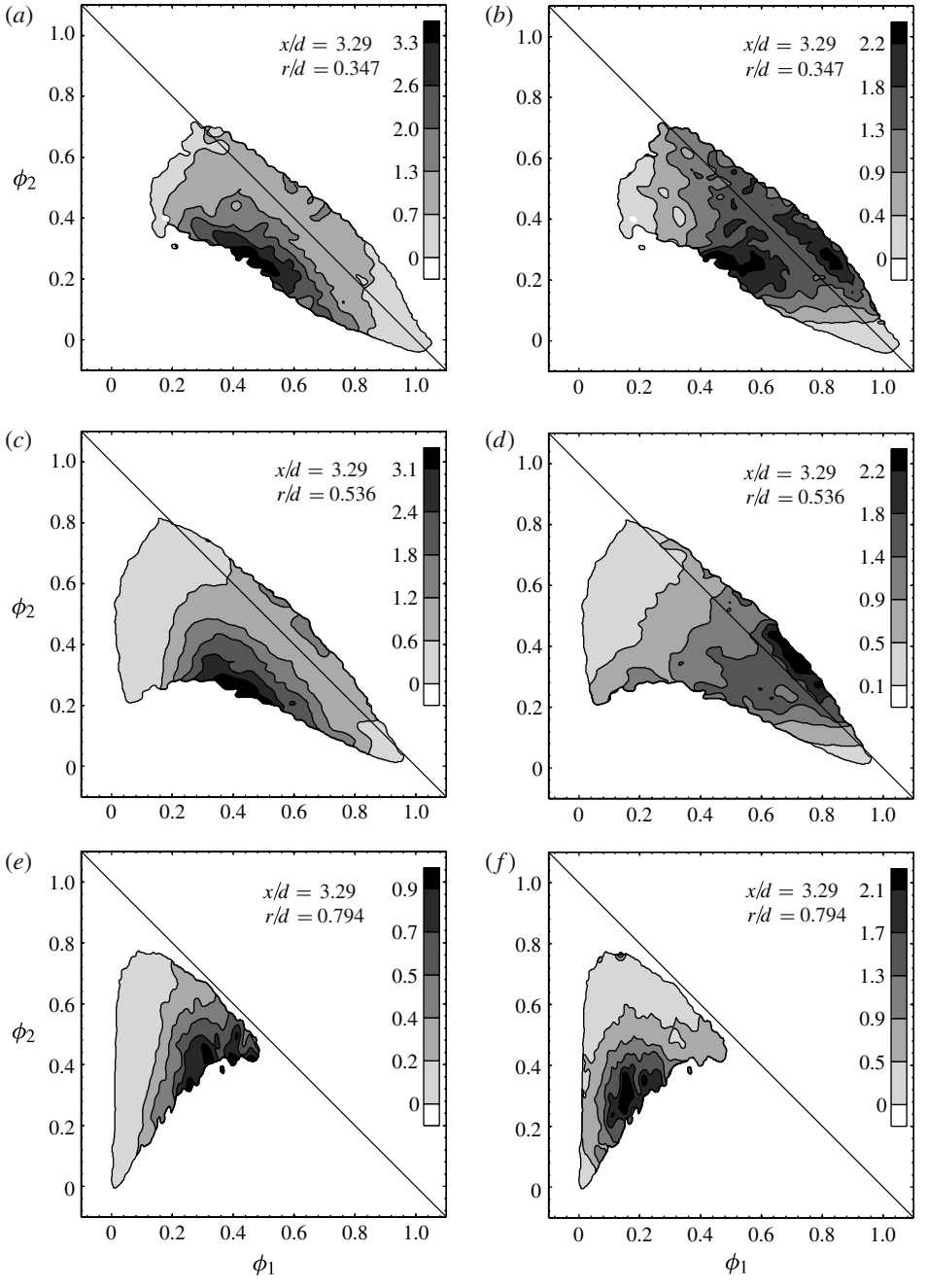

FIGURE 15. The cross-stream evolution of the conditional scalar dissipation for ϕ_1 (*a,c,e*) and ϕ_2 (*b,d,f*). The radial location is given in each figure. Conditional dissipation values are normalized by the maximum mean scalar dissipation at the same x/d location.

large-scale velocity fluctuations, indicating that there is little mixing between ϕ_1 and air. The diffusion manifold is well-defined and appears to be close to the ridgeline of the JPDF, which is also close to the conditional mean $\langle \phi_2 \mid \phi_1 \rangle$ (not shown). On the

diffusion manifold the streamlines are bell-shaped, starting near $(0, 0.4)$ and moving up to $(0.25, 0.50)$. The streamlines then bend downward towards the ϕ_1–ϕ_2 mixing line. They tend to move first in the ϕ_2 direction when approaching the manifold, suggesting that the mixing of ϕ_2 is initially much faster than that of ϕ_1. The magnitude of the diffusion velocity is large when approaching the manifold, but is much smaller on the manifold, indicating that the approach to the manifold is a much faster mixing process.

The JPDF at positions further away from the centreline (e.g. $r/d = 0.794$) becomes unimodal and extends further towards $(0, 0)$, i.e. pure air. The general streamline patterns of the conditional diffusion are opposite to those near the centreline as air becomes the dominant scalar in the mixture. For even larger r/d (not shown) the JPDF is narrow, and is approximately a straight line with a large slope starting from the origin, indicating that ϕ_2 is well mixed with a small amount of ϕ_1 because both scalars have a significant amount of time to mix when travelling outwards to reach this position, and that together they are being mixed with air.

The conditional diffusion is also affected by the measurement noise. Since the finite difference scheme used to compute the diffusion terms has a negative coefficient for the sample at the location of the computed diffusion terms, a positive noise contribution to the scalar would result in a negative diffusion value and vice versa. Because there are more samples near the peak of JPDF, the noise contributions to the diffusion cause the streamlines to converge toward the ϕ_1–ϕ_2 mixing line.

These results show that there are two mixing processes: a fast one causing the diffusion streamlines to approach the manifold, and a slow one with the streamlines moving along the manifold. Although qualitatively the fast approach to the manifold in the ϕ_2 direction is consistent with the smaller dissipation time scale for ϕ_2, quantitatively the ratio of the ϕ_2 component of the diffusion velocity to the ϕ_1 component is much larger than the dissipation time scale ratio (by at least a factor of two). The different diffusion velocities for the two scalars, therefore, cannot be explained by the dissipation time scales alone, which are a measure of the average rates of dissipation of the scalar variances. The dissipation time scales are probably a better measure of the diffusion velocity components along the manifold because the probability that the scalars are on the manifold is much higher. The fast approach to the manifold perhaps reflects the local environment in scalar and physical spaces in which the scalars mix. Specifically, the local scalar appears to be diffusing towards the ridgeline of the JPDF, which is the locally most likely composition.

In the study of Juneja & Pope (1996) the three scalars are arranged symmetrically, thereby having equal average distances from each other in scalar as well as physical space. A major difference between that study and the present work is that in the present three-scalar mixing configuration there is no direct contact between ϕ_1 and air at the jet exit. Although in scalar space the three scalars initially have equal distance from each other, the distance in physical space between ϕ_1 and air is larger than those between ϕ_1 and ϕ_2 and between ϕ_2 and air. The manifold provides a pathway along which ϕ_1 mixes with air through ϕ_2.

The conditional dissipation rates of ϕ_1 and ϕ_2 conditional on both scalars are shown in figure 15. At $x/d = 3.29$ there is little mixing on the centreline (not shown). Slightly away from the centreline (not shown) the mixing is only between ϕ_1 and ϕ_2, and the dissipation rates for both scalars are large towards $(0, 1)$. At $r/d = 0.347$ the mixing of ϕ_1 is largely among mixtures between $(1, 0)$ and $(0.2, 0.5)$, the latter likely due to the ϕ_2–air mixtures from the air side penetrating into the jet; therefore, $\langle \chi_1 \mid \phi_1 \rangle$ peaks near $\phi_1 = 0.45$ (not shown, but can be inferred from figure 15). The highest value

of $\langle \chi_1 \mid \phi_1, \phi_2 \rangle$ is near $(0.45, 0.3)$, rather than between the JPDF peaks, probably due to more intense mixing of mixtures between $(1, 0)$ and $(0.2, 0.5)$. The inward velocity fluctuations that bring the latter mixture to the location is probably much larger than the velocity fluctuations associated with the ϕ_1–ϕ_2 mixing line, thereby resulting in a sharper interface between the mixtures near $(1, 0)$ and $(0.2, 0.5)$ and large dissipation rate values. Near the mixing line, mixing is again primarily between ϕ_1 and ϕ_2. The latter does not require large velocity fluctuations to reach this location; therefore, the conditional dissipation is smaller.

In the scalar space between $(0.35, 0.6)$ and $(0.8, 0.15)$ there is also mixing between ϕ_1–ϕ_2 mixtures and ϕ_1–ϕ_2–air mixtures. The conditional dissipation is small near the ridgeline of the JPDF. This mixing scenario is likely to correspond to local events and have smaller time scales, consistent with the diffusion streamlines approaching the manifold. The conditional dissipation results are also consistent with the two different mixing processes discussed above, with the slow one related to the large-scale motions, and the fast one due to local mixing events.

The mixing of ϕ_2 at $r/d = 0.347$ is also between mixtures at $(1, 0)$ and $(0.2, 0.5)$, and $\langle \chi_2 \mid \phi_1, \phi_2 \rangle$ is quite similar to $\langle \chi_1 \mid \phi_1, \phi_2 \rangle$. This similarity is because there is little air at this location, resulting in negative correlation for ϕ_1 and ϕ_2; therefore, the process mixing ϕ_1 also mixes ϕ_2. The location for the peak of $\langle \chi_2 \mid \phi_1, \phi_2 \rangle$ is towards a slightly higher ϕ_1 value (0.5) than that of $\langle \chi_1 \mid \phi_1, \phi_2 \rangle$ (0.45), a result of mixing between ϕ_2 and air. Near $(1, 0)$, the mixture is mostly ϕ_1 and there is little mixing; therefore, the conditional dissipation rates for both ϕ_1 and ϕ_2 are small.

At $r/d = 0.536$ the conditional dissipation rates for both ϕ_1 and ϕ_2 have local peaks near $(0.45, 0.3)$, due to the mixtures at $(1, 0)$ and $(0, 0.6)$ converging to form a sharp interface. The peak dissipation occurs near the centre of the interface. In the region near $\phi_1 = 0$, mixing is primarily between ϕ_2–air mixtures having different proportions of the two. This mixing process causes the diffusion streamlines to move towards the JPDF peak near (0.1, 0.5). Near the ϕ_1–ϕ_2 mixing line, the mixing is similar to that at $r/d = 0.347$. At $r/d = 0.635$ (not shown), $\langle \chi_2 \mid \phi_1, \phi_2 \rangle$ has two peaks near $(0.15, 0.3)$ and $(0.55, 0.3)$ respectively. This location is close to that of the maximum mean ϕ_2. There is intense mixing on both sides of the maximum, one side with air and the other with ϕ_1, resulting in two dissipation peaks. Two weaker peaks also can be seen at $r/d = 0.536$, where the JPDF is bimodal; therefore, it appears that the double peaks of $\langle \chi_2 \mid \phi_1, \phi_2 \rangle$ are closely related to the bimodal JPDF. Further away from the centreline the conditional dissipation for both ϕ_1 and ϕ_2 gradually become similar because the mixing is primarily between ϕ_1–ϕ_2 mixtures and air.

The conditional cross-dissipation $\langle \chi_{12} \mid \phi_1, \phi_2 \rangle$ is shown in figure 16. Near the centreline there is little mixing; therefore, $\langle \chi_{12} \mid \phi_1, \phi_2 \rangle$ is low (not shown). At $r/d = 0.347$, mixing is primarily between ϕ_1 and ϕ_2, their gradients being strongly anti-correlated. Consequently, $\langle \chi_{12} \mid \phi_1, \phi_2 \rangle$ is negative, with the overall trend similar to those of $\langle \chi_1 \mid \phi_1, \phi_2 \rangle$ and $\langle \chi_2 \mid \phi_1, \phi_2 \rangle$. Its large magnitudes are near $(0.45, 0.3)$, coinciding with those of $\langle \chi_1 \mid \phi_1, \phi_2 \rangle$ and $\langle \chi_2 \mid \phi_1, \phi_2 \rangle$. The conditional vectorial correlation coefficient, $\langle \chi_{12} \mid \phi_1, \phi_2 \rangle / (\langle \chi_1 \mid \phi_1, \phi_2 \rangle \langle \chi_2 \mid \phi_1, \phi_2 \rangle)^{1/2}$, is close to -1, indicating a near-perfect anti-correlation. At $r/d = 0.536$, $\langle \chi_{12} \mid \phi_1, \phi_2 \rangle$ has the same qualitative features. Further away from the centreline, fluctuations of the ϕ_1 and ϕ_2 become positively correlated. At $r/d = 0.794$, $\langle \chi_{12} \mid \phi_1, \phi_2 \rangle$ has a positive peak near $(0.2, 0.3)$, coinciding with that of $\langle \chi_2 \mid \phi_1, \phi_2 \rangle$ and close to that of $\langle \chi_1 \mid \phi_1, \phi_2 \rangle$ at $(0.3, 0.4)$. The conditional vectorial correlation coefficient at $(0.2, 0.3)$ is ≈ 0.3, indicating that the ϕ_1 and ϕ_2 gradients also begin to correlate positively with each other.

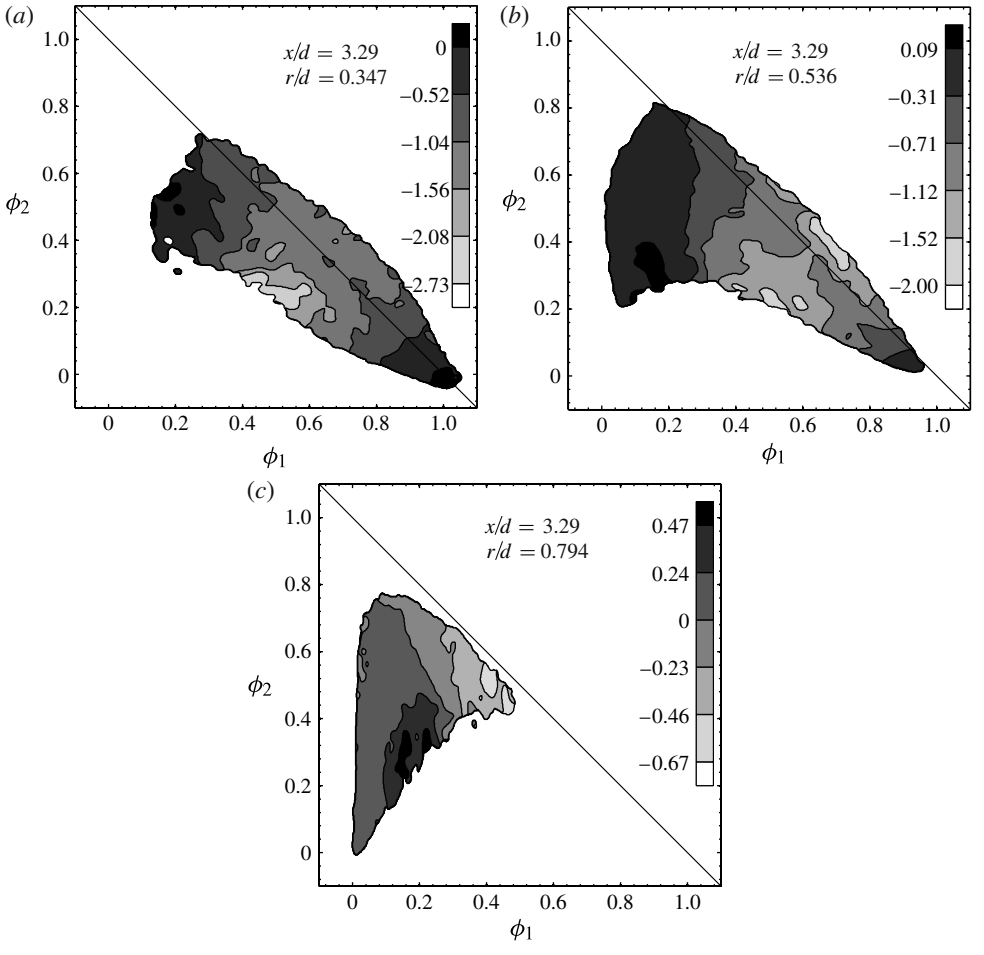

FIGURE 16. The cross-stream evolution of the conditional scalar cross-dissipation of ϕ_1 and ϕ_2. The radial location is given in each figure. Conditional cross-dissipation values are normalized by the maximum mean ϕ_1 dissipation at the same x/d location.

Moving downstream to $x/d = 6.99$, there is already air on the centreline (figure 17), Part of the JPDF ridgeline bends down from the ϕ_1–ϕ_2 mixing line, due to penetration of the ϕ_2–air mixture. Away from the centreline the JPDF bends down further towards $(0, 0)$. The peak of the JPDF shifts from the ϕ_1 side to the air side. The JPDF is only slightly bimodal at $r/d = 0.387$, indicating that the mixing has progressed much further at this downstream location. Almost pure co-flow air begins to appear near $r/d = 0.635$. At the same time, nearly pure ϕ_1 is still present. The conditional diffusion streamlines are mostly in the vertical direction before converging to the manifold. The manifold is again bell-shaped and connects mixtures having almost pure ϕ_1 and co-flow air, providing a mixing path for them. At $r/d = 0.992$, the JPDF has a tail on the ϕ_1 side, which is the opposite of that of the centreline. Further away from the centreline, ϕ_1 and ϕ_2 are well correlated, suggesting that the two scalars are brought out and mixed by the outward radial velocity fluctuations.

The conditional dissipation rates for ϕ_1 and ϕ_2 at $x/d = 6.99$ are shown in figure 18. The conditional dissipation for ϕ_1 has some similarities to that at $x/d = 3.29$ for r/d

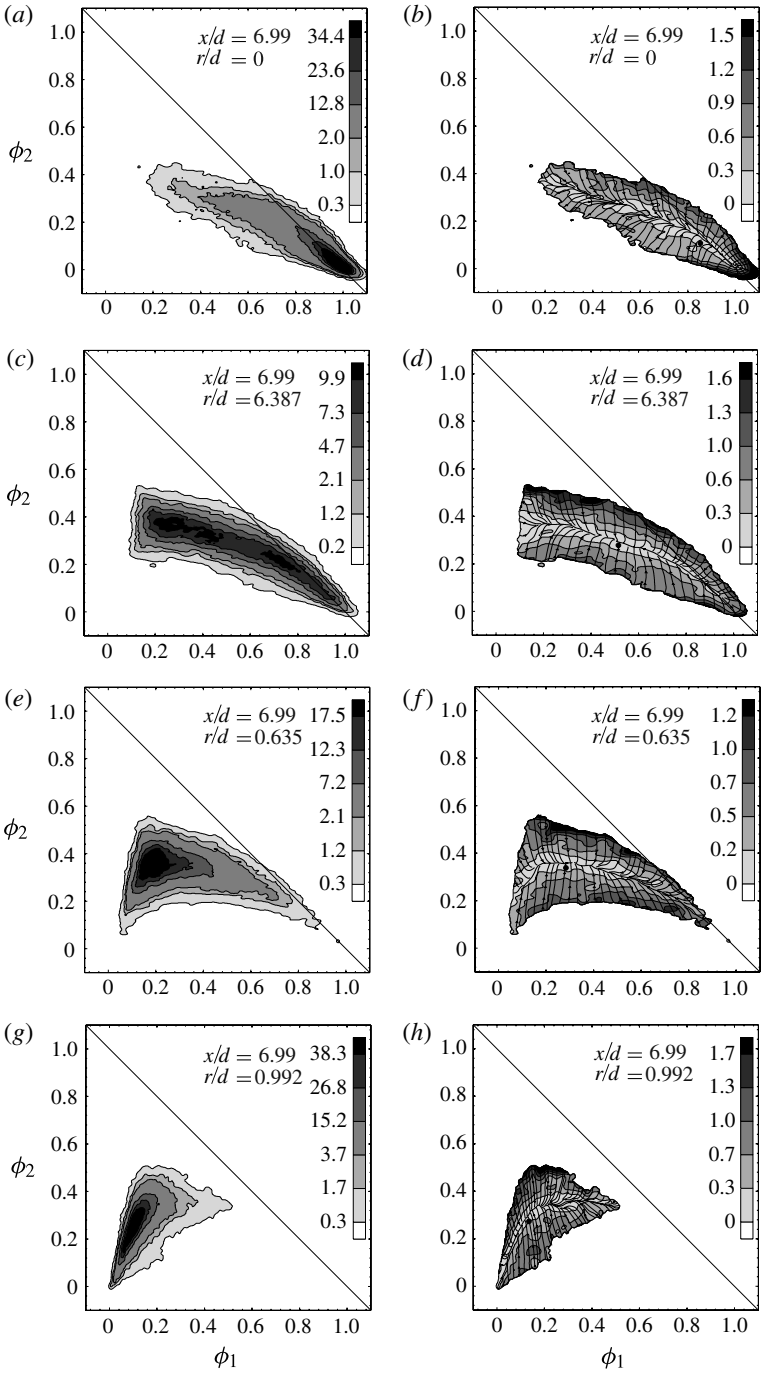

FIGURE 17. Conditions as in figure 14 but at $x/d = 6.99$.

values beyond 0.387. Near the centreline ($r/d < 0.387$), it has a maximum near (0.56, 0.16), well below the ϕ_1–ϕ_2 mixing line, again indicating that the high dissipation is caused by the large inward radial velocity fluctuations that bring mixtures from

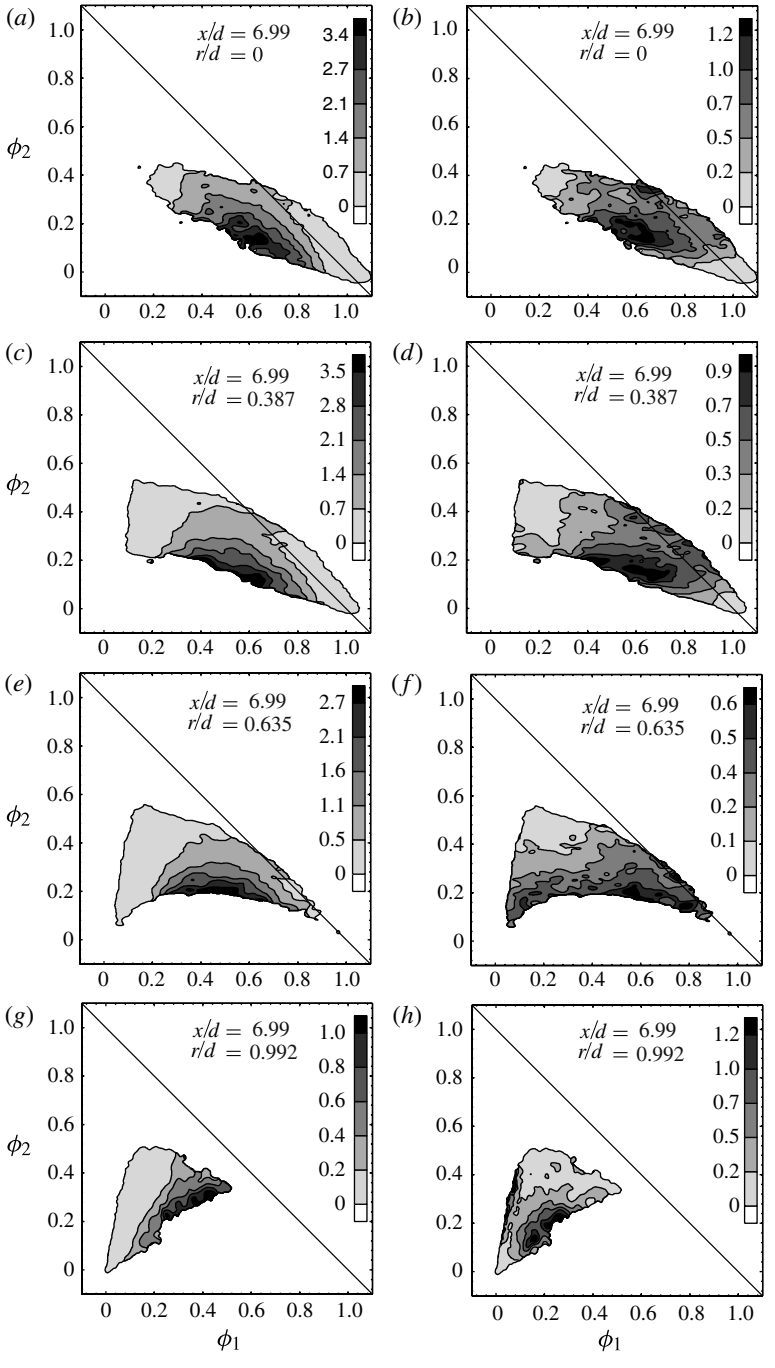

FIGURE 18. Conditions as in figure 15 but at $x/d = 6.99$.

the far air side to the measurement locations. One difference between the conditional dissipation at $x/d = 3.29$ and 6.99 is that at the latter downstream location there appear to be no minimum dissipation near the ϕ_1–ϕ_2 mixing line, probably because the probability for the mixture to be on the mixing line is small.

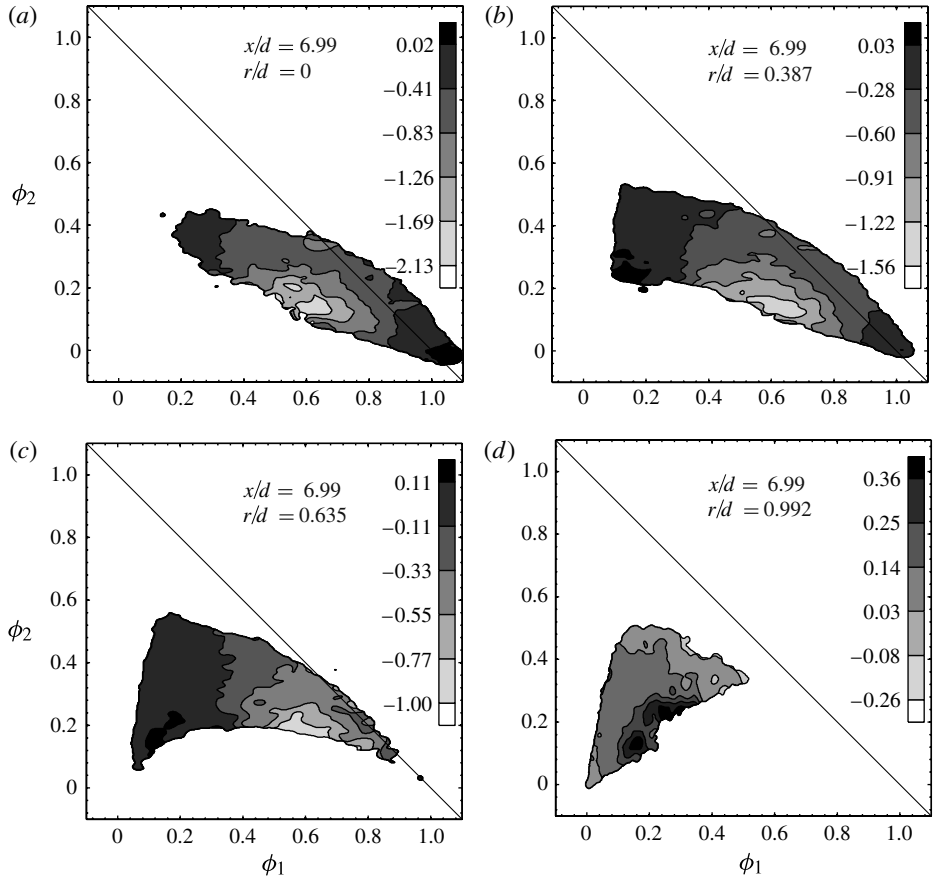

FIGURE 19. Conditions as in figure 15 but at $x/d = 6.99$.

The conditional dissipation for ϕ_2 again is similar to that of ϕ_1 near the jet centreline. The maximum is located near (0.60, 0.16), towards the ϕ_1 side compared to that of $\langle \chi_1 \mid \phi_1, \phi_2 \rangle$, consistent with the results at $x/d = 3.29$. Near the location of the maximum mean ϕ_2 ($r/d = 0.635$), $\langle \chi_2 \mid \phi_1, \phi_2 \rangle$ has two peaks, resulting from the mixing of ϕ_2 with ϕ_1 and with air, respectively.

The conditional cross-dissipation at $x/d = 6.99$ has the same general trend as that at $x/d = 3.29$. The largest negative conditional vectorial correlation coefficient is ≈ -0.8, indicating a less strong anti-correlation than at $x/d = 3.29$, due to the progression of the mixing process. At $r/d = 0.635$, the peak again coincides with that of $\langle \chi_1 \mid \phi_1, \phi_2 \rangle$ and $\langle \chi_2 \mid \phi_1, \phi_2 \rangle$, resulting from the mixing between ϕ_1 and ϕ_2. At $r/d = 0.992$, $\langle \chi_{12} \mid \phi_1, \phi_2 \rangle$ has a positive peak, indicating positive vectorial correlation for the scalar gradients.

The JPDF and conditional dissipation rates observed here have some similarities to the mixture fraction-temperature filtered mass density function and the conditionally filtered dissipation rates in turbulent flames (Cai *et al.* 2009). The JPDF is bimodal near the jet exit and becomes unimodal downstream. The filtered mass density function also has bimodal or unimodal shapes depending on the values of the conditioning variables, reflecting similar mixing processes. The conditional dissipation rate for ϕ_1 at $x/d = 3.29$ and $r/d = 0.536$ is similar to the conditionally filtered dissipation rate of

the mixture fraction (figure 2*b*,*d* in Cai *et al.* 2009). The conditional dissipation rate for ϕ_2 is similar to the conditionally filtered dissipation rate of the temperature (figure 3*b*,*d* in Cai *et al.* 2009), which also has double peaks. These similarities suggest that some of the essential properties of the mixing process in inert flows are also present in reactive flows. These properties can be used to test and improve mixing models without the complication from chemistry.

The results on the conditional diffusion also have implications for mixing models. The manifold in the diffusion velocity streamline map provides a diffusion path in scalar space. Diffusion streamlines for mixtures that are close in scalar space but separated in physical space must take a 'detour' in scalar space. Such a diffusion path presents a test for the physical-space localness for mixing models. The IEM model depends only on the scalar-space variables, and causes the scalars to move directly towards their mean values; therefore, this model cannot reproduce the detour in the scalar space.

The quick approach of the streamlines to the manifold represents a fast mixing process whereas the diffusion along the manifold is a slow process. During the fast process, the diffusion in the ϕ_2 direction often dominates. The ratio of the diffusion velocity components for ϕ_2 and ϕ_1 is larger than inverse ratio of the corresponding dissipation time scales (figure 13) (the latter probably characterize better the diffusion velocity ratio along the manifold); therefore, the fast process cannot be modelled by simply using different dissipation time scales for the two scalars (e.g. in the IEM model).

4. Conclusions

In the present study we investigated three scalar mixing in a turbulent coaxial jet. A unique aspect of this study compared to previous studies of three-scalar mixing is that two of the scalars (the centre jet and the co-flow air) are separated from the third (annulus). This configuration, therefore, better approximates the mixing process in a non-premixed turbulent reactive flows. The results provide a basis for studying multiscalar mixing in reactive flows and for testing mixing models.

The evolution of the scalar statistics along the jet centreline indicates mixing of ϕ_1 and ϕ_2 near the jet exit. Significant amounts of co-flow air begin to appear at $x/d = 7$. The correlation coefficient between the two scalars starts from a value of -1 near the jet exit and approaches unity far downstream. A high correlation indicates that two scalars are well mixed, and both are being mixed with co-flow air in unison. At this stage the three-scalar mixing is similar to two-scalar mixing. As a result, our study focused on the near field where the unique aspects of the three-scalar mixing problem are most prominent.

The radial mean scalar profiles of ϕ_1 and ϕ_2 in the near field have a centreline and an off-centreline peak, respectively. The r.m.s. fluctuations profile for ϕ_1 has an off-centreline peak approximately coinciding with location of the maximum mean ϕ_1 gradient. The r.m.s. profile for ϕ_2 has two off-centreline peaks, also coinciding with locations of the peaks of the mean ϕ_2 gradient, suggesting that production dominates the scalar variance budgets.

The correlation coefficient between ϕ_1 and ϕ_2 is close to -1 near the jet centreline, indicating an almost perfect anti-correlation. Moving away from the centreline, mixing between the two scalars and the presence of air cause the correlation to move towards positive values. Towards the edge of the jet the correlation coefficient approaches unity due to advection of mixed fluid by the large-scale flow structures.

The mean scalar dissipation profile for ϕ_1 has a peak approximately coinciding with the peak of the r.m.s. profile. The peaks of mean scalar dissipation profile for ϕ_2 also coincide with those of its r.m.s. profile. The scalar dissipation time scales vary across the jet. The highest values for ϕ_1 are approximately twice as large as for ϕ_2, probably reflecting the difference in the mean velocity between the ϕ_2 stream and the co-flow air as well as the smaller radial dimension of the ϕ_2 stream.

The scalar JPDF and the conditional dissipation rates obtained in the present study have similarities to those of mixture fraction and temperature in turbulent flames. The conditional scalar diffusion for the two scalars, shown as diffusion velocity streamlines in scalar space, generally converge quickly to a manifold along which they continue at lower velocities. The manifold appears to coincide with the ridgeline of the scalar JPDF, perhaps representing the locally most likely composition, towards which the nearby mixtures tend to diffuse.

The results also show that the approach to the manifold is generally in the ϕ_2 direction. The different magnitudes of the diffusion velocity components for the two scalars cannot be accounted for by their different dissipation time scales alone. The difference in the former is much larger. The mixing processes during the approach to the manifold, therefore, cannot be modelled by using different dissipation time scales alone.

A unique aspect of the present three-scalar mixing configuration is that while the three scalars have the same distance in scalar space, two of the scalars (ϕ_1 and air) are separated by the third (ϕ_2) in physical space. Mixing between the first two can only occur through the third, resulting in a detour of the manifold (mixing path) in scalar space. This mixing path and the approach to the manifold presents a challenging test for mixing models since most mixing models use only scalar-space variables and do not take into account the spatial (physical-space) scalar structure.

The work at Clemson was supported by the National Science Foundation under grant CBET-0651174 and the Air Force Office of Scientific Research (AFOSR) under grant FA9550-09-1-0045 (Dr J. M. Tishkoff, program manager). C.D.C. was supported by AFOSR (Dr J. M. Tishkoff, program manager). M.J.D. and C.T. were also supported by Summer Programs of the Propulsion Directorate of the Air Force Research Laboratory. We thank Professors S. Frankel and S. B. Pope for valuable discussions.

Appendix A. Noise correction for the scalar variances and scalar dissipation rates

In scalar dissipation rate measurements, it is generally necessary to correct for noise contributions and to estimate the extent to which the dissipation rate is resolved. The noise and resolution effects are usually present at the same time, with the noise contribution and resolved dissipation both increasing with resolution, making these effects difficult to separate and quantify. Cai & Tong (2009) and Cai *et al.* (2010) developed a conditional sampling-based method to separate the noise and resolution effects, to accurately correct for noise contributions, and to estimate measurement resolution. It is based on the idea that small-scale turbulent scalar is intermittent, and local fields with larger local dissipation length scales (often with lower dissipation rate values) can be selected using conditional sampling. These fields can be resolved well by the measurement system, thereby allowing separation of the noise effects and resolution effects. In the present work, we make use of the property of the conditional

dissipation that in the scalar space with low dissipation values, the dissipation length scales are larger (verified *a posteriori*). Thus, we use the scalar values ϕ_1 and ϕ_2 as conditioning variables to select well-resolved local fields. The noise contributions can be determined experimentally by computing the dissipation rate using finite difference schemes of different order, which result in different noise contributions but fully resolve the dissipation rate of the conditional samples. The noise-corrected dissipation rate is used to assess the extent to which the mean and conditional dissipation rates are resolved. The method is described briefly in the following.

A.1. *Noise variances*

In this study, the dominant noise sources are the shot noises from the Rayleigh scattering and PLIF measurements, which are additive to the scalar values. The measured scalars, ϕ_1 and ϕ_2, are

$$\phi_1 = \phi_1^* + n_{\phi_1}, \quad \phi_2 = \phi_2^* + n_{\phi_2} \tag{A 1}$$

respectively, where ϕ_1^* and ϕ_2^* are the true scalar values. The measurement noises, n_{ϕ_1} and n_{ϕ_2}, are random variables to be determined.

The shot noises at different measurement locations (different pixels) are uncorrelated with zero mean. The noise variances depend on the measured variables. In the present study ϕ_1 is obtained from PLIF measurements. Since the dependence of the fluorescence yield on ϕ_2 is much weaker than on ϕ_1, the statistics of n_{ϕ_1} should be largely a function of ϕ_1 only. We find experimentally that the dependence on ϕ_2 is indeed negligible. Furthermore, the conditional variance of n_{ϕ_1} is linear in ϕ_1, i.e.

$$\langle n_{\phi_1}^2 \mid \hat{\phi}_1, \hat{\phi}_2 \rangle = \langle n_{\phi_1}^2 \mid \hat{\phi}_1 \rangle = \alpha_0 + \alpha_1 \hat{\phi}_1, \tag{A 2}$$

where $\hat{\phi}_1$ and $\hat{\phi}_2$ are the sample-space variables for ϕ_1 and ϕ_2 respectively. The coefficient α_0 represents other possible noise that is independent of the shot noise, such as the electric noise of the camera, which is small and is important only when $\hat{\phi}_1$ approaches zero.

The noise for ϕ_2 comes from both Rayleigh scattering and PLIF. The noise from the Rayleigh measurements is proportional to the effective Rayleigh cross-section, which is a linear combination of ϕ_1 and ϕ_2,

$$\langle n_{Ray}^2 \mid \hat{\phi}_1, \hat{\phi}_2 \rangle = A_0 + A_1 \hat{\phi}_1 + A_2 \hat{\phi}_2. \tag{A 3}$$

Note that A_0 is non-zero due to Rayleigh scattering from the air in the co-flow. The ϕ_1 value measured using PLIF is used to obtain the contribution to the Rayleigh signal from ϕ_1. Since the PLIF and Rayleigh shot noises are uncorrelated, subtracting the ϕ_1 contribution from the total Rayleigh signal results in an increase in the noise variance of ϕ_2:

$$\begin{aligned} \langle n_{\phi_2}^2 \mid \hat{\phi}_1, \hat{\phi}_2 \rangle &= \langle n_{Ray}^2 \mid \hat{\phi}_1, \hat{\phi}_2 \rangle + \langle n_{aRay}^2 \mid \hat{\phi}_1, \hat{\phi}_2 \rangle \\ &= \beta_0 + \beta_1 \hat{\phi}_1 + \beta_2 \hat{\phi}_2, \end{aligned} \tag{A 4}$$

$$\langle n_{aRay}^2 \mid \hat{\phi}_1, \hat{\phi}_2 \rangle = B \langle n_{\phi_1}^2 \mid \hat{\phi}_1, \hat{\phi}_2 \rangle = B\alpha_0 + B\alpha_1 \hat{\phi}_1, \tag{A 5}$$

where $\langle n_{aRay}^2 \mid \hat{\phi}_1, \hat{\phi}_2 \rangle$ is the noise contribution to ϕ_2 from ϕ_1, and $\beta_0 = A_0 + B\alpha_0$, $\beta_1 = A_1 + B\alpha_1$ and $\beta_2 = A_2$ are coefficients to be determined using experimental data.

	α_0 ($\times 10^{-3}$)	α_1 ($\times 10^{-3}$)	β_0 ($\times 10^{-3}$)	β_1 ($\times 10^{-3}$)	β_2 ($\times 10^{-3}$)	γ_0 ($\times 10^{-3}$)	γ_1 ($\times 10^{-3}$)
$x/d = 3.29$	0.0073	0.2487	0.0308	0.0909	0.4991	−0.002 59	−0.08 611
$x/d = 6.99$	0.0055	0.2631	0.0333	0.0921	0.4327	−0.003 14	−0.090 43

TABLE 3. Noise correction coefficients. $\langle n_{\phi_1}^2 \mid \hat{\phi}_1, \hat{\phi}_2 \rangle = \alpha_0 + \alpha_1 \hat{\phi}_1$, $\langle n_{\phi_2}^2 \mid \hat{\phi}_1, \hat{\phi}_2 \rangle = \beta_0 + \beta_1 \hat{\phi}_1 + \beta_2 \hat{\phi}_2$ and $\langle n_{\phi_1} n_{\phi_2} \mid \hat{\phi}_1, \hat{\phi}_2 \rangle = \gamma_0 + \gamma_1 \hat{\phi}_1$.

A.2. *Effects of noise and determination of noise variances*

Applying the noise model discussed in the previous section to the finite difference schemes, the estimated scalar derivative is

$$\begin{aligned} h \cdot \widetilde{\frac{\mathrm{d}\phi_s}{\mathrm{d}x}} &= a_1(\phi_{s,1} - \phi_{s,-1}) + a_2(\phi_{s,2} - \phi_{s,-2}) + a_3(\phi_{s,3} - \phi_{s,-3}) \\ &\quad + a_4(\phi_{s,4} - \phi_{s,-4}) + \cdots \\ &= a_1(\phi^*_{s,1} - \phi^*_{s,-1}) + a_2(\phi^*_{s,2} - \phi^*_{s,-2}) + a_3(\phi^*_{s,3} - \phi^*_{s,-3}) + a_4(\phi^*_{s,4} - \phi^*_{s,-4}) \\ &\quad + \cdots + a_1 n_{\phi_s,1} + a_{-1} n_{\phi_s,-1} + a_2 n_{\phi_s,2} + a_{-2} n_{\phi_s,-2} + a_3 n_{\phi_s,3} + a_{-3} n_{\phi_s,-3} \\ &\quad + a_4 n_{\phi_s,4} + a_{-4} n_{\phi_s,-4} + \cdots \\ &= h \cdot \widetilde{\frac{\mathrm{d}\phi^*_s}{\mathrm{d}x}} + a_1 n_{\phi_s,1} + a_{-1} n_{\phi_s,-1} + a_2 n_{\phi_s,2} + a_{-2} n_{\phi_s,-2} + a_3 n_{\phi_s,3} + a_{-3} n_{\phi_s,-3} \\ &\quad + a_4 n_{\phi_s,4} + a_{-4} n_{\phi_s,-4} + \cdots, \end{aligned} \tag{A 6}$$

where $\widetilde{\mathrm{d}\phi^*/\mathrm{d}x}$ is the measured first derivative without noise and $s = 1, 2$ is the scalar index. Note that such an estimated derivative is dependent on the scheme used due to their different spectral responses. The measured conditional mean dissipation rate is

$$\begin{aligned} \langle \tilde{\chi}_s \mid \hat{\phi}_1, \hat{\phi}_2 \rangle &= \left\langle 2D \left(\widetilde{\frac{\mathrm{d}\phi_s}{\mathrm{d}x}} \right)^2 \middle| \hat{\phi}_1, \hat{\phi}_2 \right\rangle \\ &= \left\langle 2D \left(\widetilde{\frac{\mathrm{d}\phi^*_s}{\mathrm{d}x}} \right)^2 \middle| \hat{\phi}_1, \hat{\phi}_2 \right\rangle + \left\langle \frac{2D}{h^2} \sum_{i=-N}^{N} a_i^2 n_{\phi_s,i}^2 \middle| \hat{\phi}_1, \hat{\phi}_2 \right\rangle \\ &= \left\langle 2D \left(\widetilde{\frac{\mathrm{d}\phi^*_s}{\mathrm{d}x}} \right)^2 \middle| \hat{\phi}_1, \hat{\phi}_2 \right\rangle + \frac{2D}{h^2} \sum_{i=-N}^{N} a_i^2 \langle n_{\phi_s,i}^2 \mid \hat{\phi}_1, \hat{\phi}_2 \rangle \\ &= \left\langle 2D \left(\widetilde{\frac{\mathrm{d}\phi^*_s}{\mathrm{d}x}} \right)^2 \middle| \hat{\phi}_1, \hat{\phi}_2 \right\rangle \\ &\quad + \frac{2D}{h^2} \sum_{i=-N}^{N} a_i^2 \langle f_s(\phi_{1,i}, \phi_{2,i}) \mid \phi_{1,0} = \hat{\phi}_1, \phi_{2,0} = \hat{\phi}_2 \rangle \\ &\backsimeq \left\langle 2D \left(\widetilde{\frac{\mathrm{d}\phi^*_s}{\mathrm{d}x}} \right)^2 \middle| \hat{\phi}_1, \hat{\phi}_2 \right\rangle \end{aligned}$$

$$
\begin{aligned}
&+\frac{2D}{h^2}\sum_{i=-N}^{N} a_i^2\langle f_s(\phi_{1,0},\phi_{2,0}) \mid \phi_{1,0}=\hat{\phi}_1,\phi_{2,0}=\hat{\phi}_2\rangle \\
&=\left\langle 2D\left(\widetilde{\frac{\mathrm{d}\phi_s^*}{\mathrm{d}x}}\right)^2 \middle| \hat{\phi}_1,\hat{\phi}_2\right\rangle+\frac{2D}{h^2}\sum_{i=-N}^{N} a_i^2\langle n_{\phi_s}^2 \mid \hat{\phi}_1,\hat{\phi}_2\rangle \\
&=\left\langle 2D\left(\widetilde{\frac{\mathrm{d}\phi_s^*}{\mathrm{d}x}}\right)^2 \middle| \hat{\phi}_1,\hat{\phi}_2\right\rangle+\frac{2D}{h^2}C_N\langle n_{\phi_s}^2 \mid \hat{\phi}_1,\hat{\phi}_2\rangle \qquad \text{(A 7)}
\end{aligned}
$$

where $C_N=\sum_{i=-N}^{N} a_i^2$, D, $2D(\widetilde{\mathrm{d}\phi^*/\mathrm{d}x})^2$ and $f_s(\phi_1,\phi_2)$ are a scheme-dependent coefficient, the scalar diffusivity, the noise-corrected dissipation rate and the variance model for the n_{ϕ_s} respectively. The approximation from the fourth to the fifth line is made with a Taylor series expansion of f_s about the centre point of the scheme and keeping the first-order term:

$$
\begin{aligned}
\sum_{i=-N}^{N} a_i^2 f_s(\phi_{1,i},\phi_{2,i}) &= \sum_{i=-N}^{N} a_i^2 f_s(\phi_1(x_0+\mathrm{i}h),\phi_2(x_0+\mathrm{i}h)) \\
&=\sum_{i=-N}^{N} a_i^2\left\{f_s(\phi_1(x_0),\phi_2(x_0))+\left.\frac{\mathrm{d}f_s}{\mathrm{d}x}\right|_{x_0}\mathrm{i}h+\frac{i^2h^2}{2}\left.\frac{\mathrm{d}^2f_s}{\mathrm{d}x^2}\right|_{x_0}+o(h^3)\right\} \\
&=\sum_{i=-N}^{N} a_i^2\left\{f_s(\phi_1(x_0),\phi_2(x_0))+\frac{i^2h^2}{2}\left.\frac{\mathrm{d}^2f_s}{\mathrm{d}x^2}\right|_{x_0}+o(h^3)\right\} \\
&=\sum_{i=-N}^{N} a_i^2\left\{f_s(\phi_1(x_0),\phi_2(x_0))+\frac{i^2h^2}{2}\sum_{j=1}^{2}\left.\frac{\partial f_s}{\partial\phi_j}\frac{\partial^2\phi_j}{\partial x^2}\right|_{x_0}+o(h^3)\right\}.
\end{aligned}
\qquad \text{(A 8)}
$$

In the last step, the linear dependence of f_s on ϕ_j is used. The numerical schemes can affect the measured conditional dissipation rates in two ways. Firstly, higher-order schemes can resolve more dissipation rates. Secondly, higher schemes result in higher noise contributions. We use the second property to determine the noise variances as follows.

At any given point in the scalar space, i.e. given ϕ_1 and ϕ_2 values, when all the schemes (or schemes of certain order or higher) can resolve the scalar fields, the resolved dissipation rate (the first term on the last line of (A 7)) is independent of the scheme used, while the measured dissipation rate depends bilinearly with respect to the conditional noise variance and C_N, the latter depending on the scheme used. The conditional noise variance can be regarded as a coefficient in the $\langle\tilde{\chi}_s \mid \hat{\phi}_1,\hat{\phi}_2\rangle - C_N$ (linear) relationship, which is employed to estimate the conditional noise variance, by varying C_N using schemes of different orders. Repeating the above procedure, the estimated conditional noise variance is obtained for all the occupied region in scalar space. The model in the previous section ((A 2) and (A 4)) is then fitted to the conditional noise variance using the linear least-squares method to obtain α_0, α_1, β_0, β_1 and β_2. After the noise variance is determined, (A 7) is used to correct the conditional scalar dissipation rate.

The mean (unconditioned) dissipation rate can be corrected in the same way. For example, the measured $\langle\tilde{\chi}_2\rangle$ is

$$\begin{aligned}
\langle\tilde{\chi}_2\rangle &= \left\langle 2D\left(\widetilde{\frac{\mathrm{d}\phi_2}{\mathrm{d}x}}\right)^2\right\rangle \\
&= \left\langle 2D\left(\widetilde{\frac{\mathrm{d}\phi_2^*}{\mathrm{d}x}}\right)^2\right\rangle + \left\langle \frac{2D}{h^2}\sum_{i=-N}^{N} a_i^2 n_{\phi_2,i}^2\right\rangle \\
&= \left\langle 2D\left(\widetilde{\frac{\mathrm{d}\phi_2^*}{\mathrm{d}x}}\right)^2\right\rangle + \frac{2D}{h^2}\sum_{i=-N}^{N} a_i^2\langle n_{\phi_2,i}^2\rangle \\
&= \left\langle 2D\left(\widetilde{\frac{\mathrm{d}\phi_2^*}{\mathrm{d}x}}\right)^2\right\rangle + \frac{2D}{h^2}\sum_{i=-N}^{N} a_i^2\langle f_2(\phi_{1,i},\phi_{2,i})\rangle \\
&\backsimeq \left\langle 2D\left(\widetilde{\frac{\mathrm{d}\phi_2^*}{\mathrm{d}x}}\right)^2\right\rangle + \frac{2D}{h^2}\sum_{i=-N}^{N} a_i^2\langle f_2(\phi_{1,0},\phi_{2,0})\rangle \\
&= \left\langle 2D\left(\widetilde{\frac{\mathrm{d}\phi_2^*}{\mathrm{d}x}}\right)^2\right\rangle + \frac{2D}{h^2}\sum_{i=-N}^{N} a_i^2\langle n_{\phi_2}^2\rangle \\
&= \left\langle 2D\left(\widetilde{\frac{\mathrm{d}\phi_2^*}{\mathrm{d}x}}\right)^2\right\rangle + \frac{2D}{h^2}C_N\langle n_{\phi_2}^2\rangle \\
&= \left\langle 2D\left(\widetilde{\frac{\mathrm{d}\phi_2^*}{\mathrm{d}x}}\right)^2\right\rangle + \frac{2D}{h^2}C_N(\beta_0+\beta_1\langle\phi_1\rangle+\beta_2\langle\phi_2\rangle). \qquad \text{(A 9)}
\end{aligned}$$

The coefficients β_0, β_1, β_2 are the same as in (A 4).

We find that the scalar dissipation rates are fully resolved except when $\langle\chi_1 \mid \phi_1,\phi_2\rangle$ or $\langle\chi_2 \mid \phi_1,\phi_2\rangle$ peaks. Based on the ratio of the noise-corrected dissipation ratios using the 8th- and 10th-order schemes (typically greater than 99 %), we conclude that these large dissipation values are 98 % or better resolved.

The cross-dissipation can also be corrected in a similar way. Here the noise covariance, $\langle n_{\phi_1}n_{\phi_2} \mid \phi_1,\phi_2\rangle$, which comes from subtracting the Rayleigh signal from acetone from the total to obtain that from ethylene, needs to be determined. The noise covariance can be written in the form $\langle n_{\phi_1}n_{\phi_2} \mid \hat{\phi}_1,\hat{\phi}_2\rangle = \gamma_0+\gamma_1\hat{\phi}_1$. The coefficients, γ_0 and γ_1, are determined using the same method for those in $\langle n_{\phi_1}^2 \mid \hat{\phi}_1,\hat{\phi}_2\rangle$ and $\langle n_{\phi_2}^2 \mid \hat{\phi}_1,\hat{\phi}_2\rangle$.

Appendix B. Uncertainty analysis

The uncertainties in the scalar statistics come from several sources. They include the uncertainties in determining the acetone source concentration, the imaging camera response and the laser profiles, and the uncertainties in statistical analysis (due to finite sample size). The first three are system uncertainties and can be estimated by examining the scalar JPDF on the centreline at $x/d = 3.29$. The JPDF, if free from noise, should be limited to the $(0,1)$ and $(1,0)$ mixing line. Both noise and uncertainties cause the JPDF to broaden. Using the Gaussian JPDF as an

approximation, the 99 % contour is at approximately three standard deviations. Thus the r.m.s. fluctuations of the combined noise and uncertainty are $\approx 0.06/3 = 0.02$ (2 % of the full scale of ϕ_1). Assuming that the uncertainties are independent of the noise, the r.m.s. fluctuations of the uncertainties are $(0.02^2 - 0.016^2)^{1/2} = 0.012$, where the $n_{\phi_1} = 0.016$ at $\phi_1 = 1$ is obtained in Appendix A. The 1.2 % uncertainty appears to be consistent with the accuracies of various apparatus and experimental conditions.

The maximum statistical uncertainties in the mean scalar profiles are estimated using the peak r.m.s. fluctuations (0.24 from figure 8) as $\sigma_1/\sqrt{N} = 0.24/\sqrt{3000} = 0.0044$, where $N = 3000$ is the number of images (independent samples). Thus, the uncertainties are dominated by system uncertainties. The statistical uncertainties in the r.m.s. fluctuations (σ_1) are estimated in a similar way. The ratio of the r.m.s. of the measured variance to the variance is $((k-1)/(N-1))^{1/2} = 0.0258$, leading to a ratio of the r.m.s. of σ_1 to σ_1 of 0.013, where $k = 3$ is the approximate value of the kurtosis of the scalar fluctuations. This uncertainty is comparable to the system uncertainty. The combined uncertainty is $(0.012^2 + 0.013^2)^{1/2} = 0.0178$.

The mean dissipation rates and the cross-dissipation rate are averaged over 3 pixels and 5 pixels in the radial and axial directions, respectively, to improve statistical convergence. The resulting r.m.s. uncertainty for the maximum $\langle \chi_1 \rangle$ is $\sigma_{\langle \chi_1 \rangle} = \sigma_{\chi_1}/\sqrt{N} = 47.65/\sqrt{45000} = 0.2246$, which is about 0.85 % of the peak $\langle \chi_1 \rangle$ value. The relative uncertainty, $\sigma_{\langle \chi_1 \rangle}/\langle \chi_1 \rangle$, at other radial locations is also close to 1 %. The averaging in the radial direction results in a bias of ≈ 0.5 % for the maximum $\langle \chi_1 \rangle$. The uncertainty and bias for $\langle \chi_2 \rangle$ are also similar.

The scalar JPDF is affected by the measurement noise, the statistical uncertainty, and bias. Noise broadens the JPDF. Deconvolution can be used to correct independent noise. The noise in the present work, however, depends on the scalar values ((A 2), (A 4)). Thus no attempt is made to correct the noise effects.

The statistical uncertainty and bias are estimated using the bootstrap method (Hall 1990). The r.m.s. values of the JPDF are typically less than 4 % of the JPDF values for much of the sample space, and are less than 10 % near the contour for 90 % integrated probability, only rising to 18 % at the 99 % probability contour. The bias is typically less than 3 % (negative) near the JPDF peak(s) and is less than 6 % at the 90 % contour, again rising to 15 % at the 99 % contour. The combined (mean-square) error is less than 4 %, 10 % and 23 % respectively.

The statistical uncertainty and bias for the conditional dissipation rates are estimated using the method given by Ruppert (1997). The r.m.s. uncertainties for both $\langle \chi_1 \mid \phi_1, \phi_2 \rangle$ and $\langle \chi_2 \mid \phi_1, \phi_2 \rangle$ are typically less than 3 % of the dissipation rates, only rising to ≈ 10 % in the highest dissipation regions of the sample space, which are usually near the 90 % integrated JPDF contour. The bias is typically less than 5 % for $\langle \chi_1 \mid \phi_1, \phi_2 \rangle$ and 3 % for $\langle \chi_2 \mid \phi_1, \phi_2 \rangle$, rising to ≈ 15 % in high dissipation regions.

REFERENCES

ANTONIA, R. A., TEITEL, M., KIM, J. & BROWNE, L. W. B. 1992 Low-Reynolds-number effects in a fully developed turbulent channel flow. *J. Fluid Mech.* **236**, 579–605.

ANTONOPOULOS-DOMIS, M. 1981 Large-eddy simulation of a passive scalar in isotropic turbulence. *J. Fluid Mech.* **104**, 55–79.

BAILEY, S. C. C., HULTMARK, M., SCHUMACHER, J., YAKHOT, V. & SMITS, A. J. 2009 Measurement of local dissipation scales in turbulent pipe flow. *Phys. Rev. Lett.* **103**, 014502.

BALARAC, G., SI-AMEUR, M., LESIEUR, M. & MÉTAIS, O. 2007 Direct numerical simulations of high velocity ratio coaxial jets: mixing properties and influence of upstream conditions. *J. Turbul.* **8** (22), 1–27.

BURESTI, G., PETAGNA, P. & TALAMELLI, A. 1998 Experimental investigation on the turbulent near-field of coaxial jets. *Exp. Therm. Fluid Sci.* **17**, 18–36.

CAI, J., BARLOW, R. S., KARPETIS, A. N. & TONG, C. 2010 Noise correction and length scale estimation for scalar dissipation rate measurements in turbulent partially premixed flames. *Flow Turbul. Combust.* **85**, 309–332.

CAI, J. & TONG, C. 2009 A conditional-sampling-based method for noise and resolution corrections for scalar dissipation rate measurements. *Phys. Fluids* **21**, 065104.

CAI, J., WANG, D., TONG, C., BARLOW, R. S. & KARPETIS, A. N. 2009 Investigation of subgrid-scale mixing of mixture fraction and temperature in turbulent partially premixed flames. *Proc. Combust. Inst.* **32**, 1517–1525.

DAHM, W. J. A & DIMOTAKIS, P. E. 1990 Mixing at large Schmidt number in the self-similar far field of turbulent jets. *J. Fluid Mech.* **217**, 299–330.

DOWLING, D. R. & DIMOTAKIS, P. E. 1990 Similarity of concentration field of gas-phase turbulent jets. *J. Fluid Mech.* **218**, 109.

DRAKE, M. C., PITZ, R. W. & SHYY, W. 1986 Conserved scalar probability functions on a turbulent jet flame. *J. Fluid Mech.* **171**, 27–51.

EFFELSBERG, E. & PETERS, N. 1983 A composite model for the conserved scalar PDF. *Combust. Flame* **50**, 351–360.

ESWARAN, V. & POPE, S. B. 1988 Direct numerical simulations of the turbulent mixing of a passive scalar. *Phys. Fluids* **31** (3), 506–520.

GAO, F. 1991 An analytical solution for the scalar probability density-function in homogeneous turbulence. *Phys. Fluids* A **3**, 511–513.

HALL, P. 1990 Using the bootstrap to estimate mean squared error and select smoothing parameter in nonparametric problems. *J. Multivariate Anal.* **32**, 177–203.

HOLZER, M. & PUMIR, A. 1993 Simple models of non-Gaussian statistics for a turbulently advected passive scalar. *Phys. Rev.* E **47**, 202–219.

JABERI, F. A., MILLER, R. S., MADNIA, C. K. & GIVI, P. 1996*a* Non-Gaussian scalar statistics in homogeneous turbulence. *J. Fluid Mech.* **313**, 241–282.

JABERI, F. A., MILLER, R. S. & GIVI, P. 1996*b* Conditional statistics in turbulent scalar mixing and reaction. *AIChE J.* **42**, 1149–1152.

JANICKA, J. & KOLLMANN, W. 1979 A two-variables formalism for the treatment of chemical reaction in turbulent H_2-air diffusion flames. In *Seventh Symposium (International) on Combustion*, pp. 421–430.

JAYESH, & WARHAFT, Z. 1991 Probability-distribution of a passive scalar in grid-generated turbulence. *Phys. Rev. Lett.* **67**, 3503–3506.

JAYESH, & WARHAFT, Z. 1992 Probability distribution, conditional dissipation, and transport of passive temperature fluctuations in grid-generated turbulence. *Phys. Fluids* A **4**, 2292–2307.

JUNEJA, A. & POPE, S. B. 1996 A DNS study of turbulent mixing of two passive scalars. *Phys. Fluids* **8**, 2161–2184.

KAILASNATH, P., SREENIVASAN, K. R. & SAYLOR, J. R. 1993 Conditional scalar dissipation rates in turbulent wakes, jets, and boundary layers. *Phys. Fluids* **5**, 3207–3215.

KERSTEIN, A. R. & MCMURTRY, P. A. 1994 Mean-field theories of random advection. *Phys. Rev.* E **49**, 474–482.

KOMORI, S., HUNT, J. C. R., KANZAKI, T. & MURAKAMI, Y. 1991 The effects of turbulent mixing on the correlation between two species and on concentration fluctuations in non-premixed reacting flows. *J. Fluid Mech.* **228**, 629–659.

LAVERTU, R. A. & MYDLARSKI, L. 2005 Scalar mixing from a concentrated source in turbulent channel flow. *J. Fluid Mech.* **528**, 135–172.

LEONARD, A. D. & HILL, J. C. 1991 Scalar dissipation and mixing in turbulent reacting flows. *Phys. Fluids* A **3**, 1286–1299.

LOCKWOOD, F. C. & MONEIB, H. A. 1980 Fluctuating temperature measurements in a heated round free jet. *Combust. Sci. Technol.* **22**, 209–224.

LOCKWOOD, F. C. & NAGUIB, A. S. 1975 The prediction of the fluctuations in the properties of free, round-jet, turbulent, diffusion flames. *Combust. Flame* **24**, 109–124.

MA, B. & WARHAFT, Z. 1986 Some aspects of the thermal mixing layer in grid turbulence. *Phys. Fluids* **29**, 3114–3120.

MI, J., ANTONIA, R. A. & ANSELMET, F. 1995 Joint statistics between temperature and its dissipation rate components in a round jet. *Phys. Fluids* **7**, 1665–1673.

MILLER, R. S., FRANKEL, S. H., MADNIA, C. K. & GIVI, P. 1993 Johnson–Edgeworth translation for probability modelling of binary mixing in turbulent flows. *Combust. Sci. Technol.* **91**, 21–52.

O'BRIEN, E. E. & JIANG, T. L. 1991 The conditional dissipation rate of an initially binary scalar in homogeneous turbulence. *Phys. Fluids* A **3**, 3121–3123.

OVERHOLT, M. R. & POPE, S. B. 1996 Direct numerical simulation of a passive scalar with imposed mean gradient in isotropic turbulence. *Phys. Fluids* **8**, 3128–3148.

POPE, S. B. 1985 PDF methods for turbulent reacting flows. *Prog. Energy Combust. Sci.* **11**, 119–192.

POPE, S. B. & CHING, E. 1993 Stationary probability density function in turbulence. *Phys. Fluids* A **5**, 1529–1531.

PRAUSNITZ, J. M., POLING, B. E. & O'CONNELL, J. P. 2001 *The Properties of Gases and Liquids*. McGraw-Hill.

PUMIR, A., SHRAIMAN, B. & SIGGIA, E. D. 1991 Exponential tails and random advection. *Phys. Rev. Lett.* **66**, 2984–2987.

REID, R. C., PRAUSNITZ, J. M. & POLING, B. E. 1989 *The Properties of Gases and Liquids*. McGraw-Hill.

RHODES, R. P. 1975 *Turbulent Mixing in Non-reactive and Reactive Flows*. Plenum.

RUPPERT, D. 1997 Empirical-bias bandwidths for local polynomial nonparametric regression and density estimation. *J. Am. Stat. Assoc.* **92**, 1049–1062.

SABEL'NIKOV, V. A. 1998 Asymptotic solution of the equation for the probability distribution of a passive scalar in grid turbulence with a uniform mean scalar gradient. *Phys. Fluids* **10**, 743–755.

SAHAY, A. & O'BRIEN, E. E. 1993 Uniform mean scalar gradient in grid turbulence: conditioned dissipation and production. *Phys. Fluids* A **5**, 1076–1078.

SHRAIMAN, B. I. & SIGGIA, E. D. 1994 Lagrangian path-integrals and fluctuations in random flow. *Phys. Rev.* E **49**, 2912–2927.

SINAI, Y. G. & YAHKOT, V. 1989 Limiting probability distribution of a passive scalar in a random velocity field. *Phys. Rev. Lett.* **63**, 1962–1964.

SIRIVAT, A. & WARHAFT, Z. 1982 The mixing of passive helium and temperature fluctuations in grid turbulence. *J. Fluid Mech.* **120**, 475–504.

SREENIVASAN, K. R. & ANTONIA, R. A. 1978 Joint probability densities and quadrant contributions in a heated turbulent round jet. *AIAA J.* **16**, 867–868.

SREENIVASAN, K. R., TAVOULARIS, S., HENRY, R. & CORRSIN, S. 1980 Temperature fluctuations and scales in grid-generated turbulence. *J. Fluid Mech.* **100**, 597–621.

TAVOULARIS, S. & CORRSIN, S. 1981 Experiments in nearly homogeneous turbulent shear flow with a uniform mean temperature gradient. Part 2. The fine structure. *J. Fluid Mech.* **104**, 349–367.

TAYLOR, A. M. K. P. 1993 *Instrumentation for Flows with Combustion*. Academic.

TONG, C. & WARHAFT, Z. 1995 Scalar dispersion and mixing in a jet. *J. Fluid Mech.* **292**, 1–38.

VENKATARAMANI, K. S. & CHEVRAY, R. 1978 Statistical features of heat-transfer in grid-generated turbulence: constant-gradient case. *J. Fluid Mech.* **86**, 513–543.

VENKATARAMANI, K. S., TUTU, N. K. & CHEVRAY, R. 1975 Probability distributions in a round turbulent jet. *Phys. Fluids* **18**, 1413–1420.

VILLERMAUX, E. & REHAB, H. 2000 Mixing in coaxial jets. *J. Fluid Mech.* **425**, 161–185.

WAND, M. P. & JONES, M. C. 1995 *Kernel Smoothing*. Chapman & Hall.

WANG, G. H. & CLEMENS, N. T. 2004 Effects of imaging system blur on measurements of flow scalars and scalar gradients. *Exp. Fluids* **37**, 194–205.

WARHAFT, Z. 1981 The use of dual heat injection to infer scalar covariance decay in grid turbulence. *J. Fluid Mech.* **104**, 93–109.

WARHAFT, Z. 1984 The interference of thermal fields from line sources in grid turbulence. *J. Fluid Mech.* **144**, 363–387.

WARHAFT, Z. & LUMLEY, J. L. 1978 An experimental study of the decay of temperature fluctuations in grid-generated turbulence. *J. Fluid Mech.* **88**, 659–684.

YEUNG, P. K. 1998 Correlations and conditional statistics in differential diffusion: scalars with uniform mean gradients. *Phys. Fluids* **10**, 2621–2635.